ARTICLE

Structure and mechanism of the cation–chloride cotransporter NKCC1

Thomas A. Chew[1,2,9], Benjamin J. Orlando[3,9], Jinru Zhang[1,9], Naomi R. Latorraca[1,2,4,5,6], Amy Wang[1,4,5,6,7], Scott A. Hollingsworth[1,4,5,6,8], Dong-Hua Chen[6], Ron O. Dror[1,2,4,5,6], Maofu Liao[3]* & Liang Feng[1,2,6]*

Cation–chloride cotransporters (CCCs) mediate the electroneutral transport of chloride, potassium and/or sodium across the membrane. They have critical roles in regulating cell volume, controlling ion absorption and secretion across epithelia, and maintaining intracellular chloride homeostasis. These transporters are primary targets for some of the most commonly prescribed drugs. Here we determined the cryo-electron microscopy structure of the Na–K–Cl cotransporter NKCC1, an extensively studied member of the CCC family, from *Danio rerio*. The structure defines the architecture of this protein family and reveals how cytosolic and transmembrane domains are strategically positioned for communication. Structural analyses, functional characterizations and computational studies reveal the ion-translocation pathway, ion-binding sites and key residues for transport activity. These results provide insights into ion selectivity, coupling and translocation, and establish a framework for understanding the physiological functions of CCCs and interpreting disease-related mutations.

CCCs mediate coupled movement of Cl^- with K^+ and/or Na^+ across the membrane and are critical for maintaining K^+, Na^+ and Cl^- homeostasis[1–4]. CCCs have important roles in physiological processes, including regulating volume and blood pressure and modulating hearing and neuronal excitability[1,4,5]. This family can be divided into two main clades[1–3,6]: clade I is Na^+ dependent and includes the $Na^+–K^+–Cl^-$ cotransporters NKCC1 and NKCC2, and the $Na^+–Cl^-$ cotransporter NCC. Clade II is independent of Na^+ and includes the $K^+–Cl^-$ cotransporter KCC1-4[2,6]. Malfunction or dysregulation of CCCs results in disorders including hypertension, fluid overload and kidney filtration problems[1]. Mutations of CCCs cause Gitelman syndrome, Bartter syndrome and Andermann syndrome[1].

Many widely prescribed medications target Na^+-dependent CCCs[7]. Thiazide diuretics, the preferred first-line pharmacological therapy for hypertension, inhibit NCC[8]. Furosemide, bumetanide and other loop diuretics commonly prescribed for acute oedema target NKCC[9]. Despite decades of clinical use of major drugs targeting CCCs, the molecular mechanisms underlying ion transport and drug inhibition remain unclear.

CCCs consist of a transmembrane domain (TMD), which contains the ion-translocation pathway, and cytosolic N- and C-terminal domains (NTD and CTDs, respectively), which regulate transport and trafficking[10,11]. CCCs mediate electroneutral movement of cotransported ions. A common structural scaffold gives rise to diverse stoichiometries for different family members: $1Na^+$:$1K^+$:$2Cl^-$ for NKCCs, $1Na^+$:$1Cl^-$ for NCC and $1K^+$:$1Cl^-$ for KCC[1]. Substrate specificity and coupling stoichiometry are central to interpreting physiological functions of CCCs. Major advances in physiological, biochemical, biophysical, genetic and cellular studies provide a basis for understanding their function and malfunction[10,12,13]. However, fundamental questions remain, including regarding ion selectivity, transport coupling and cytosolic regulation.

Here we report the cryo-electron microscopy (cryo-EM) structure of a vertebrate NKCC1 from *D. rerio*. The structure, together with functional studies and molecular dynamics simulations, defines the architecture of this family of transporters and provides insight into its regulation and mechanisms of ion translocation.

Structure determination

We focused on the Na^+-dependent NKCC1, an extensively studied CCC[2,14]. NKCC1 has important roles in regulating cell volume, intracellular Cl^- concentration and trans-epithelial salt secretion[1,2]. Moreover, NKCC1 is a promising neurological drug target, owing to its importance in GABAergic signalling[15]. We determined that zebrafish NKCC1 (*Dr*NKCC1) showed desirable properties for structural studies (Extended Data Fig. 1a–c).

*Dr*NKCC1 and human NKCC1 (*Hs*NKCC1) sequences share 71% identity and 87% similarity (Supplementary Fig. 1). Similar to mouse NKCC1, loss of function of *Dr*NKCC1 leads to endolymph collapse[16,17]. Cells overexpressing wild-type *Dr*NKCC1 showed robust Rb^+ (a classic K^+ congener) influx (Fig. 1e). Influx was minimized by substituting an equivalent residue critical for *Hs*NKCC1 activity[18] or by addition of the NKCC inhibitor bumetanide. Thus, *Dr*NKCC1 recapitulates key characteristics of *Hs*NKCCs.

Cryo-EM analyses of full-length and NTD-truncated *Dr*NKCC1 generated similar 3D reconstructions with well-resolved TMD and CTD (Extended Data Fig. 1, 2). Full-length NKCC1 yielded a higher-resolution map, and is therefore the focus of our structural analyses. To overcome substantial CTD conformational flexibility (Extended Data Fig. 2), we used multi-body refinement, producing electron microscopy maps with clear side-chain densities for unambiguous model building (Extended Data Fig. 3). TMD-focused image processing produced a 2.9 Å-resolution map, revealing several ion-binding sites, which are discussed below.

[1]Department of Molecular and Cellular Physiology, Stanford University School of Medicine, Stanford, CA, USA. [2]Biophysics Program, Stanford University, Stanford, CA, USA. [3]Department of Cell Biology, Harvard Medical School, Boston, MA, USA. [4]Department of Computer Science, Stanford University, Stanford, CA, USA. [5]Institute for Computational and Mathematical Engineering, Stanford University, Stanford, CA, USA. [6]Department of Structural Biology, Stanford University School of Medicine, Stanford, CA, USA. [7]Department of Chemical Engineering, Stanford University, Stanford, CA, USA. [8]Present address: Merck & Co., South San Francisco, CA, USA. [9]These authors contributed equally: Thomas A. Chew, Benjamin J. Orlando, Jinru Zhang. *e-mail: maofu_liao@hms.harvard.edu; liangf@stanford.edu
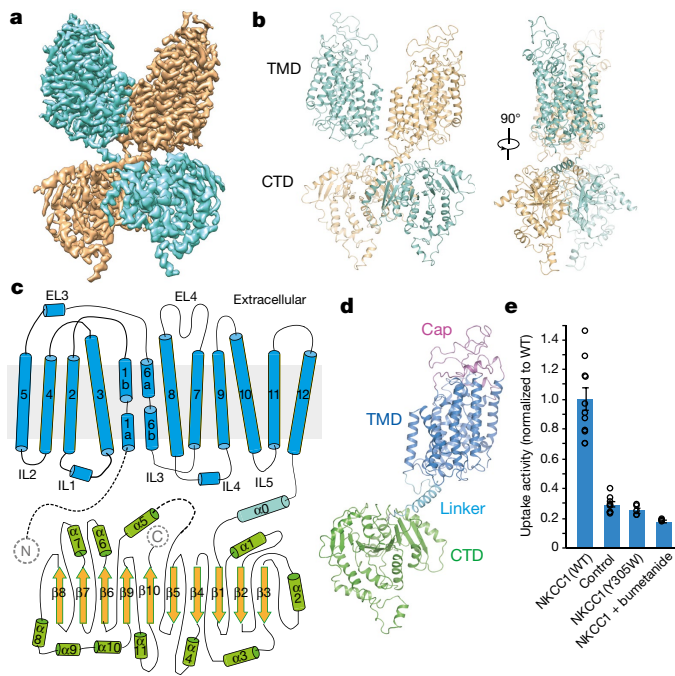
Fig. 1 | Overall structure and functional characterization of NKCC1. **a**, Full-length NKCC1 density map coloured by protomer. **b**, Overall structure of the NKCC1 dimer. Ribbon representations viewed at two angles. **c**, Topology diagram of NKCC1. **d**, Ribbon representation of NKCC1 protomer, coloured by structural element. **e**, Uptake activities of *Dr*NKCC1. The activity was normalized to the wild-type transporter (WT) (mean ± s.e.m., $n = 4$ independent experiments except for wild type and unrelated protein control, $n = 10$ independent experiments). EL, extracellular loop.

Our cryo-EM structures reveal a dimeric assembly of NKCC1, consistent with previous crosslinking and FRET studies[19,20]. The twofold axis of the TMDs is perpendicular to the membrane surface whereas that of the CTDs is tilted by ~11°. The CTD of one subunit is close to the TMD of the opposing subunit, showing a domain-swap configuration. Multi-body analysis revealed several modes of motion between TMD and CTD (Extended Data Fig. 4), including swivelling and rocking (Supplementary Videos 1, 2, 3).

Transmembrane domain

The TMD adopts an APC superfamily fold, with an inverted repeat architecture formed by transmembrane segment (TM)1–TM5 and TM6–TM10[12,21] (Fig. 1c). NKCC1 shares limited structural similarity with other transporter families beyond the basic protein fold. Its top-ranked hit (DALI comparison) is a distantly related bacterial amino acid transporter, GkApcT (C_α root mean square deviation (r.m.s.d.) = 3.2 Å for 399 out of 1,136 residues; 15% sequence identity). NKCC1 has two substantial extracellular elements: an extensive ordered loop between TM7 and TM8 (EL4) stabilized by a conserved disulfide bond and a structured element between TM5 and TM6 (EL3). These elements form a cap domain, shielding the extracellular surface of the TMD (Figs. 1d, 2a). The cap domain is important for surface expression and transport regulation in *Hs*NKCC1[22].

Two TMDs interact through an interface formed by TM11, TM12 and the TM10 C-terminal end (Fig. 2c, d), consistent with bioinformatic predictions[18]. However, the TMD-dimer interface shows only modest shape complementarity in the membrane near the cytoplasm. Three lipid molecules in the inner membrane leaflet were observed at the dimer interface (Fig. 2c, d). One lipid molecule inserts both tails into a central cavity, whereas the other two lipids each have one acyl tail wedged into the side cavity, acting like molecular glue to fill gaps and bridge interactions between the two TMDs. These observations
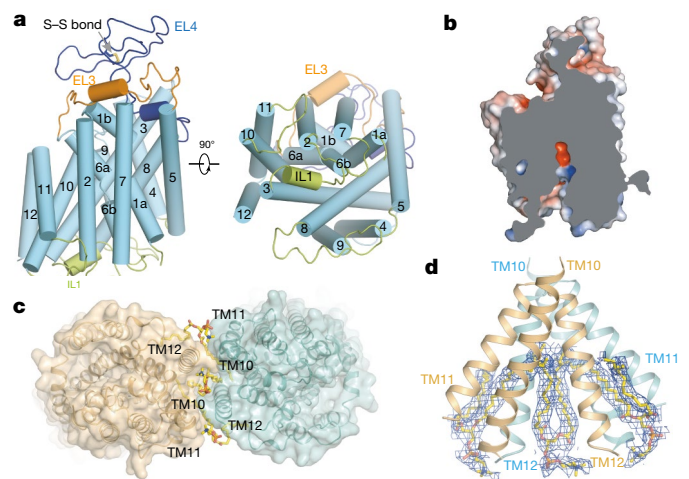

Fig. 2 | TMD and dimer interface. a, TMD structure in one subunit, viewed from the membrane (left) or the intracellular side (right). **b**, Slab view of one TMD showing a partially inward-open conformation. The surface is coloured by electrostatic potential (red, -5 kT e^{-1}; blue, $+5$ kT e^{-1}). **c**, Lipids and dimer of TMDs, viewed from the intracellular side. **d**, Ordered lipid molecules at the dimer interface. Densities attributed to lipids are shown as blue meshes.

provide direct evidence of interfacial lipids, which have been proposed to have important roles in membrane protein oligomerization and association[23].

Cytosolic domains and TMD–CTD interface

The NTD has variable length and limited sequence conservation[24,25]. In the 3D reconstruction of full-length NKCC1, the NTD lacked discernible density, indicating disordered structure or conformational flexibility. The NTD apparently does not make stable direct contacts with the TMD or CTDs. The TMD and CTD adopt similar conformations to the NTD-truncated protein. The structural basis of the role of the NTD in NKCC1 activation awaits future investigation.

Large, conserved CTDs are characteristic of CCCs. The CTD has key roles in protein folding, membrane trafficking, quaternary structure maintenance and transport regulation[26–28]. NKCC1 activation is accompanied by large movements of the CTD; in KCC, CTD phosphorylation results in deactivation[28,29].

The CTD core adopts a mixed α/β fold with two structurally related subdomains (Extended Data Fig. 5a). Despite limited sequence conservation (identity <12%), each CTD of NKCC1 resembles that of MaCCC (a prokaryotic CCC transporter)[30]. Compared with MaCCC, the NKCC1 CTD contains several large loops and additional helices, substantially increasing the surface area for potential interactions.

The two CTDs within the NKCC1 dimer directly interact (Extended Data Fig. 5b), consistent with the CTD affecting dimerization[26,28]. Cross-protomer interactions are mainly mediated by helix α3, its subsequent loop, and strand β3. The CTD-dimer interface is distinct from the one that was proposed on the basis of the isolated MaCCC soluble domain[30]. A region previously linked to dimerization participates in this interface, corroborating our structure[31]. The interface between two CTDs is relatively small without cross-interface hydrogen bonds, making it potentially flexible for structural rearrangement. Changes in interface packing could potentially result in significant movements in distant regions, as suggested by past FRET studies[20,28].

The TMD and CTD are connected by an α-helix with a linker, comprising around ten residues, on each end (Fig. 1d). The helix from one subunit packs against that of the other, a region we term the 'scissor helix', owing to its shape and structural role. This scissor helix crosses below the TMD-dimer interface, bringing the CTD of one protomer under the TMD of its neighbouring protomer, producing a domain-swapped architecture. The scissor helix sits in a groove formed by its
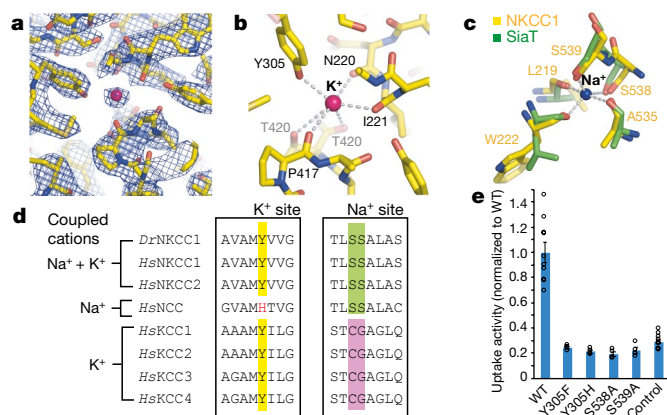
Fig. 3 | K⁺- and Na⁺-binding sites. a, K⁺-binding site density map (10.0σ, blue mesh). Strong additional density is attributed to K⁺ (pink sphere). **b**, K⁺-binding site. Dashed lines denote possible coordination. **c**, Na⁺-binding site. The proposed Na⁺-binding site (yellow) of NKCC1 is superimposed onto the Na2 site of (green) SiaT. Dashed lines denote the Na⁺ coordination in SiaT. **d**, The sequence alignment around key K⁺- or Na⁺-coordinating residues of human and zebrafish CCCs. Highlighted positions show Y305 (K⁺-coordinating), S538 and S539 (Na⁺-coordinating). **e**, Uptake activities of NKCC1 with mutations in the substrate-binding pocket, normalized to wild type (mean ± s.e.m., $n = 4$ independent experiments; wild type and control are the same as in Fig. 1e).

neighbouring scissor helix and the CTD (Extended Data Fig. 5b), contributing substantially to the dimer interface.

Multi-body refinement revealed transient interactions between the CTD and TMD (Extended Data Fig. 4). The intracellular loop and the short helix IL1 between TM2 and TM3 contact the N-terminal end of the scissor helix and the C terminus of the CTD (Extended Data Fig. 5c). Additionally, the intracellular loop IL5 is in close proximity to the loop after helix α1. The multiple contacts with the TMD by cytosolic elements provide potential mechanisms to regulate transport by restricting conformational transitions in the TMD. The intracellular surface of the TMD is mostly positively charged except near the dimer interface (Extended Data Fig. 5d). NTD phosphorylation might facilitate interaction with the positively charged intracellular surface of the TMD, potentially leading to activation. Substituting residues that make prominent contacts at the TMD–cytosolic domain interface (TMD Arg630; cytosolic Asn682, Ser686) abolished transport (Extended Data Fig. 6a–d), suggesting that TMD–cytosolic domain communication has an important role.

Ion transport pathway and cation-binding sites

In our structure, *Dr*NKCC1 is captured in a partially inward-open conformation (Fig. 2b). A solvent-accessible vestibule—surrounded mainly by TM1, TM3, TM6 and TM8—extends from the intracellular surface into the TMD (Fig. 2b). Near the end of the vestibule, the electrostatic surface is highly negative. After a narrow restriction point approximately 8 Å into the vestibule, the electrostatic surface becomes positive. These electrostatic properties might provide a local environment that accommodates different substrate ions. As the vestibule widens half-way towards the intracellular side, its electrostatic distribution shows sidedness, suggesting that cations and anions may take separate routes to reach substrate-binding sites.

Cryo-EM samples contained K⁺, Na⁺ and Cl⁻. The strongest non-protein density (around 20σ) is roughly spherical and located within the typical substrate-binding pocket in APC transporters (Fig. 3a), which we ascribe to a substrate ion. Several lines of evidence suggest that this ion is K⁺. First, its negatively charged environment and coordination by multiple backbone carbonyls suggest a cation. Second, it is directly coordinated by the hydroxyl group of Tyr305, which is strictly conserved in K⁺-transporting NKCC and KCC but not in K⁺-independent NCC (which contains histidine instead)[12] (Fig. 3d).

The conservation of Tyr305 in NKCC and KCC but not in NCC is likely to reflect a functional requirement, given the low sequence similarity between NKCC and KCC (approximately 18%) compared to NKCC and NCC (approximately 50%) (Supplementary Fig. 1). Thus, the most plausible ion is K⁺.

The K⁺ is located close to the helical breaks of TM1 and TM6 and is coordinated by the Tyr305 side-chain oxygen and main-chain carbonyls from Asn220, Ile221, Pro417 and Thr420 (Fig. 3b). The approximately 2.94 Å average coordination distance is much closer to the average reported for K⁺ (2.84 Å) than for Na⁺ (2.42 Å)[32]. Additionally, the Thr420 side-chain oxygen is about 3.8 Å from K⁺ and might contribute to K⁺ binding.

The Na⁺-binding site called Na2 is conserved across many APC transporters[33–36]. An equivalent site is found in NKCC1. When superimposed onto the Na2 of SiaT, a well-characterized Na⁺-coupled sialic acid transporter, all Na⁺-coordinating elements were positioned nearly identically[36] (Fig. 3c). We therefore propose that this is the Na⁺-binding site in NKCC1. Like SiaT, the backbone carbonyls of two TM1 residues (Leu219 and Trp222), one TM8 residue (Ala535) and the side-chain oxygen of two consecutive TM8 serines (Ser538 and Ser539) would directly coordinate Na⁺. Both Ser538 and Ser539 are strictly conserved in Na⁺-transporting NKCCs and NCC, whereas cysteine and glycine are typically found in Na⁺-independent KCCs (Fig. 3d). This sequence analysis corroborates the proposed Na⁺-binding site. In the cryo-EM map, we observe a weak non-protein density barely above background levels at this position, insufficient for unambiguous ion placement. We speculate that this might reflect a partially occupied or loosely bound state. This would be in line with the partially inward-open conformation depicted in our structure, given that the Na2 site is often disrupted in a fully inward-open conformation of other APC transporters[37].

To validate proposed ion-binding sites, we performed mutagenesis (Fig. 3e, Extended Data Fig. 6b–d). Substituting Ser538 or Ser539 reduced transport to background levels. Mutating Tyr305 to tryptophan, histidine or a more conserved phenylalanine abolished transport, confirming previous mutagenesis studies in *Hs*NKCC1[18]. These results are consistent with our structural observations.

Molecular dynamics simulations and Cl⁻-binding sites

To better understand the translocation pathway and identify potential Cl⁻-binding sites, we performed all-atom molecular dynamics simulations on the TMD. In simulations initiated with bound K⁺ and Na⁺, both cations typically remained in their respective binding pockets for hundreds of nanoseconds. In nearly all these simulations, but not in simulations lacking bound cations, Cl⁻ from the bulk solvent spontaneously bound in a solvent-accessible region of the transporter (Extended Data Table 2).

Visualizing the Cl⁻ probability densities in simulations revealed at least three binding regions (Fig. 4a). Cl⁻ ions first diffused into the TMD between TM1 and TM6b (Fig. 4b, bottom), remaining here transiently before exiting intracellularly or moving deeper into the cavity. In some simulations, Cl⁻ explored an additional intracellular region between TM6b and TM10 (Fig. 4b, middle). In a small fraction of simulations, Cl⁻ diffused into a region between TM1 and TM6a, above the K⁺-binding site (Fig. 4b, top). At most, two chloride ions bound in any of these three regions at once (Extended Data Fig. 7). Among the three potential Cl⁻-binding sites, two are deep in the translocation pathway and resemble Cl⁻-coordinating sites in other transporters with adjacent main-chain amide coordination (Fig. 4b, top and middle), leading to stable binding in simulations. By contrast, the site closest to the intracellular bulk solvent (Fig. 4b, bottom) coordinated Cl⁻ less tightly through side-chain interactions. We reasoned that this represents a transient site, akin to a third lower-affinity site in 2Cl⁻:1H⁺ CLC transporters[38], whereas the other two sites are likely to mediate coupled 1Na⁺:1K⁺:2Cl⁻ transport.

We initiated further simulations with both cations bound and with chloride ions bound at the two stable Cl⁻-binding regions (Fig. 4b, top and middle). In slightly over half of simulations, the top Cl⁻ shifted
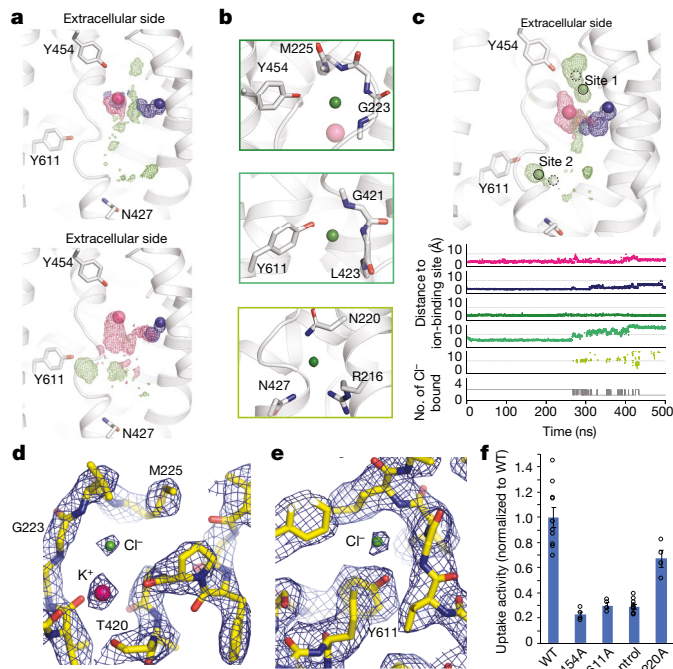
Fig. 4 | Cl⁻-binding sites. a, Probability density for K^+ (pink), Na^+ (blue) and Cl^- (green) across two simulations initiated with bound cations. Spheres indicate the initial position of cations. **b**, Three regions of Cl^- binding are identified in simulation. **c**, Top, ion probability densities, as shown in **a**, for a simulation initiated with all four ions bound. The initial position of K^+, Na^+ and Cl^- are indicated as pink, blue and green (with dashed boundaries) spheres, respectively. The positions of Cl^-, based on the cryo-EM map, are indicated by green spheres with solid boundaries. Bottom, the first five traces show distance from the ion-binding site to the nearest ion of that type (see Methods). In the presence of stably bound chlorides, cations reside longer within the translocation pore. Light grey lines at 5 Å offer a visual guide. The bottom trace shows a number of chlorides occupying the Cl^--binding sites. **d**, Density map of the top Cl^--binding site (site 1) and the K^+-binding site (11.0σ, blue mesh). **e**, Density map of the bottom Cl^--binding site (site 2) (6.0σ, blue mesh). **f**, Uptake activities of mutant transporters, normalized to wild type (mean ± s.e.m., $n = 4$ independent experiments; wild type and control are same as in Fig. 1e).

away from Tyr454 to form an electrostatic interaction with K^+ (Fig. 4c), matching well with a strong electron density (around 18σ) close to the K^+ density (around 20σ) (Fig. 4c, d). We therefore propose that K^+ and the main-chain amides from Val224 and Met225 constitute a primary Cl^--binding site ('site 1'). In simulation, the bottom Cl^- shifted to coordinate with main-chain amides at positions 421–423 and the side chain of Tyr611 (Fig. 4c). Again, this shifted position ('site 2') matches with a strong non-protein electron density (around 9σ) in this region (Fig. 4c, e). Two proposed Cl^- densities and the K^+ density are the strongest non-protein and non-lipid densities in the cryo-EM map. Both Cl^- densities are located in highly positively charged environments and coordinated by backbone amides in helical breaks, bearing similarity to CLC transporter Cl^--binding sites[38]. Together, the results of our cryo-EM and simulations suggest that these two sites represent bona fide Cl^--binding sites.

Simulations initiated with K^+ and Na^+ bound—but not with only either K^+ or Na^+ bound—showed frequent Cl^- binding to the more intracellular Cl^- site (site 2), suggesting that both cations are needed to facilitate Cl^- binding (Extended Data Fig. 8d). Additional simulations suggest that in the presence of two chlorides, K^+ is more stabilized than Na^+ (Extended Data Fig. 8c), in line with EM observations (Extended Data Fig. 8e). Swapping the initial placement of K^+ and Na^+ generally reduced the stability of each ion (Extended Data Fig. 8a, b). In one such simulation, K^+ escaped, and then Na^+ spontaneously moved to
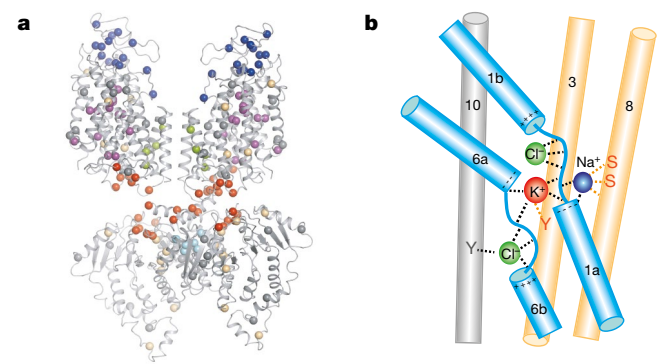

Fig. 5 | Disease-related mutations and interconnected ion-binding sites. a, Mutations in NCC linked to Gitelman syndrome mapped onto the structure by sequence alignment. Mutations are shown as spheres and grouped into six categories: ion-translocation pathway (purple), cap domain (blue), TMD-dimer interface (green), TMD–soluble domain interface (red), CTD-dimer interface (cyan), and structural or folding (yellow) mutations. Other mutations are shown in grey. **b**, Schematic of ion-binding sites. Dashed lines, coordination; light blue, core domain helices; yellow, scaffold domain helices.

the proposed Na^+ site (Extended Data Fig. 8e). These results support cooperative ion binding and the K^+- and Na^+-binding site assignments.

To probe the roles of the proposed Cl^--coordinating residues, we performed mutagenesis studies (Fig. 4f, Extended Data Fig. 6b–d). Replacing Tyr611 diminished activity, consistent with its important role in coordinating the bottom Cl^-. Of note, mutating Tyr454 also abolished uptake, suggesting its involvement with the top Cl^- during transport. Mutating Asn220 compromised activity, but to a lesser extent, in line with its proposed role in forming a transient site visited en route to stable binding sites. These results are consistent with our structural and computational observations regarding the location and make-up of Cl^--binding sites.

Disease-related mutations

Given the sequence and functional conservation among NKCCs and NCC, the *Dr*NKCC1 structure provides a framework for interpretation of disease-related mutations in Na^+-dependent CCC transporters[1,12].

Few *Hs*NKCC1 mutations have been discovered, probably owing to its diverse functions and essential roles in development. Here, we focused on mutations in NCC, the CCC with the largest number of known mutations[1], which is associated with Gitelman syndrome[39]. We mapped these known mutations onto the NKCC1 structure[1,40], grouping them into six categories (Fig. 5a, Supplementary Table 1): (1) mutations in the ion-translocation pathway, expected to affect transport; (2) cap mutations, suggesting an important role in transporter function or folding; (3) TMD-dimer interface mutations, may affect interactions with the other protomer or interfacial lipids; (4) TMD–soluble interface mutations that might affect domain interactions. The enrichment of cytosolic mutations near the TMD-soluble interface suggests an important role of TMD–CTD communication in regulating transport; (5) CTD-dimer interface mutations that might affect CTD interactions and communication; (6) Structural mutations, such as those replacing glycine, introducing proline or replacing bulky hydrophobic residues with charged ones, which are likely to cause destabilization or affect folding.

Discussion

Dimerization has been found in a variety of transporter families, and is implicated in regulating transport[41]. In transporters with cytosolic regulatory domains such as NKCCs, TMD–cytosolic domain linkers are often flexible. The geometrical constraints imposed by dimerization can help maintain proximity between cytosolic domains and TMDs, thereby facilitating communication to regulate transport. It remains unknown whether two protomers of NKCC1 communicate during transport.

Our structural observations shed light on ion coupling (Fig. 5b). The Na$^+$- and K$^+$-binding sites are in close proximity and form between the core and scaffold domains, where their disruption or formation could be cooperative during state transitions. The top Cl$^-$ is mainly coordinated by backbone amides in the TM1-hinge region, adjacent to K$^+$- and Na$^+$-coordinating residues. It is conceivable that K$^+$ and Na$^+$ binding could stabilize the hinge conformation for Cl$^-$ coordination, and vice versa. Furthermore, the top Cl$^-$ is within range to interact with K$^+$, suggesting cooperative binding. The residues coordinating the bottom Cl$^-$ are adjacent to K$^+$-coordinating residues in the same TM6 hinge region. Thus, the physical proximity and connectedness between Na$^+$-, K$^+$- and Cl$^-$-binding sites suggest a potential mechanism for ion coupling and cooperative binding.

To our knowledge, this structure of NKCC1 represents the first structure of an APC transporter that contains a cytosolic regulatory domain. The alternating access of APC transporters typically involves pronounced movement of the core domain relative to the scaffold domain. Comparable conformational transitions in NKCC1 are expected to cause substantial changes in the intracellular regions of the TMD at the interface with the CTD. In addition, some degree of flexibility between the CTD and TMD as observed in our structures could enable different relative orientations or engagement according to states. These features might facilitate CTD–TMD communication, regulating transport activity. Further research is needed to determine the detailed mechanism of regulation by the CTD.

Online content

1. Gamba, G. Molecular physiology and pathophysiology of electroneutral cation–chloride cotransporters. *Physiol. Rev.* **85**, 423–493 (2005).
2. Haas, M. & Forbush, B., III. The Na–K–Cl cotransporter of secretory epithelia. *Annu. Rev. Physiol.* **62**, 515–534 (2000).
3. Arroyo, J. P., Kahle, K. T. & Gamba, G. The SLC12 family of electroneutral cation-coupled chloride cotransporters. *Mol. Aspects Med.* **34**, 288–298 (2013).
4. Russell, J. M. Sodium–potassium–chloride cotransport. *Physiol. Rev.* **80**, 211–276 (2000).
5. Kaila, K., Price, T. J., Payne, J. A., Puskarjov, M. & Voipio, J. Cation–chloride cotransporters in neuronal development, plasticity and disease. *Nat. Rev. Neurosci.* **15**, 637–654 (2014).
6. Gagnon, K. B. & Delpire, E. Physiology of SLC12 transporters: lessons from inherited human genetic mutations and genetically engineered mouse knockouts. *Am. J. Physiol. Cell Physiol.* **304**, C693–C714 (2013).
7. Duarte, J. D. & Cooper-DeHoff, R. M. Mechanisms for blood pressure lowering and metabolic effects of thiazide and thiazide-like diuretics. *Expert Rev. Cardiovasc. Ther.* **8**, 793–802 (2010).
8. ALLHAT Officers and Coordinators for the ALLHAT Collaborative Research Group. Major outcomes in high-risk hypertensive patients randomized to angiotensin-converting enzyme inhibitor or calcium channel blocker vs diuretic: The Antihypertensive and Lipid-Lowering Treatment to Prevent Heart Attack Trial (ALLHAT). *J. Am. Med. Assoc.* **288**, 2981–2997 (2002).
9. Schrier, R. W. Use of diuretics in heart failure and cirrhosis. *Semin. Nephrol.* **31**, 503–512 (2011).
10. Markadieu, N. & Delpire, E. Physiology and pathophysiology of SLC12A1/2 transporters. *Pflug. Arch.* **466**, 91–105 (2014).
11. Flemmer, A. W., Gimenez, I., Dowd, B. F., Darman, R. B. & Forbush, B. Activation of the Na–K–Cl cotransporter NKCC1 detected with a phospho-specific antibody. *J. Biol. Chem.* **277**, 37551–37558 (2002).
12. Hartmann, A. M. & Nothwang, H. G. Molecular and evolutionary insights into the structural organization of cation chloride cotransporters. *Front. Cell. Neurosci.* **8**, 470 (2015).
13. Payne, J. A. Molecular operation of the cation chloride cotransporters: ion binding and inhibitor interaction. *Curr. Top. Membr.* **70**, 215–237 (2012).
14. Gamba, G. et al. Molecular cloning, primary structure, and characterization of two members of the mammalian electroneutral sodium–(potassium)–chloride cotransporter family expressed in kidney. *J. Biol. Chem.* **269**, 17713–17722 (1994).
15. Yamada, J. et al. Cl$^-$ uptake promoting depolarizing GABA actions in immature rat neocortical neurones is mediated by NKCC1. *J. Physiol.* **557**, 829–841 (2004).
16. Abbas, L. & Whitfield, T. T. Nkcc1 (Slc12a2) is required for the regulation of endolymph volume in the otic vesicle and swim bladder volume in the zebrafish larva. *Development* **136**, 2837–2848 (2009).
17. Flagella, M. et al. Mice lacking the basolateral Na–K–2Cl cotransporter have impaired epithelial chloride secretion and are profoundly deaf. *J. Biol. Chem.* **274**, 26946–26955 (1999).
18. Somasekharan, S., Tanis, J. & Forbush, B. Loop diuretic and ion-binding residues revealed by scanning mutagenesis of transmembrane helix 3 (TM3) of Na–K–Cl cotransporter (NKCC1). *J. Biol. Chem.* **287**, 17308–17317 (2012).
19. Moore-Hoon, M. L. & Turner, R. J. The structural unit of the secretory Na$^+$–K$^+$–2Cl$^-$ cotransporter (NKCC1) is a homodimer. *Biochemistry* **39**, 3718–3724 (2000).
20. Pedersen, M., Carmosino, M. & Forbush, B. Intramolecular and intermolecular fluorescence resonance energy transfer in fluorescent protein-tagged Na–K–Cl cotransporter (NKCC1): sensitivity to regulatory conformational change and cell volume. *J. Biol. Chem.* **283**, 2663–2674 (2008).
21. Yamashita, A., Singh, S. K., Kawate, T., Jin, Y. & Gouaux, E. Crystal structure of a bacterial homologue of Na$^+$/Cl$^-$-dependent neurotransmitter transporters. *Nature* **437**, 215–223 (2005).
22. Ye, Z. Y., Li, D. P., Byun, H. S., Li, L. & Pan, H. L. NKCC1 upregulation disrupts chloride homeostasis in the hypothalamus and increases neuronal activity-sympathetic drive in hypertension. *J. Neurosci.* **32**, 8560–8568 (2012).
23. Gupta, K. et al. The role of interfacial lipids in stabilizing membrane protein oligomers. *Nature* **541**, 421–424 (2017).
24. Isenring, P. & Forbush, B. III. Ion and bumetanide binding by the Na–K–Cl cotransporter. Importance of transmembrane domains. *J. Biol. Chem.* **272**, 24556–24562 (1997).
25. Gagnon, K. B., England, R. & Delpire, E. A single binding motif is required for SPAK activation of the Na–K–2Cl cotransporter. *Cell. Physiol. Biochem.* **20**, 131–142 (2007).
26. Parvin, M. N., Gerelsaikhan, T. & Turner, R. J. Regions in the cytosolic C-terminus of the secretory Na$^+$–K$^+$–2Cl$^-$ cotransporter NKCC1 are required for its homodimerization. *Biochemistry* **46**, 9630–9637 (2007).
27. Nezu, A., Parvin, M. N. & Turner, R. J. A conserved hydrophobic tetrad near the C terminus of the secretory Na$^+$–K$^+$–2Cl$^-$ cotransporter (NKCC1) is required for its correct intracellular processing. *J. Biol. Chem.* **284**, 6869–6876 (2009).
28. Monette, M. Y. & Forbush, B. Regulatory activation is accompanied by movement in the C terminus of the Na–K–Cl cotransporter (NKCC1). *J. Biol. Chem.* **287**, 2210–2220 (2012).
29. Rinehart, J. et al. Sites of regulated phosphorylation that control K–Cl cotransporter activity. *Cell* **138**, 525–536 (2009).
30. Warmuth, S., Zimmermann, I. & Dutzler, R. X-ray structure of the C-terminal domain of a prokaryotic cation-chloride cotransporter. *Structure* **17**, 538–546 (2009).
31. Parvin, M. N. & Turner, R. J. Identification of key residues involved in the dimerization of the secretory Na$^+$–K$^+$–2Cl$^-$ cotransporter NKCC1. *Biochemistry* **50**, 9857–9864 (2011).
32. Harding, M. M. Metal-ligand geometry relevant to proteins and in proteins: sodium and potassium. *Acta Crystallogr. D* **58**, 872–874 (2002).
33. Krishnamurthy, H., Piscitelli, C. L. & Gouaux, E. Unlocking the molecular secrets of sodium-coupled transporters. *Nature* **459**, 347–355 (2009).
34. Faham, S. et al. The crystal structure of a sodium galactose transporter reveals mechanistic insights into Na$^+$/sugar symport. *Science* **321**, 810–814 (2008).
35. Weyand, S. et al. Structure and molecular mechanism of a nucleobase-cation-symport-1 family transporter. *Science* **322**, 709–713 (2008).
36. Wahlgren, W. Y. et al. Substrate-bound outward-open structure of a Na$^+$-coupled sialic acid symporter reveals a new Na$^+$ site. *Nat. Commun.* **9**, 1753 (2018).
37. Perez, C., Koshy, C., Yildiz, O. & Ziegler, C. Alternating-access mechanism in conformationally asymmetric trimers of the betaine transporter BetP. *Nature* **490**, 126–130 (2012).
38. Dutzler, R., Campbell, E. B. & MacKinnon, R. Gating the selectivity filter in ClC chloride channels. *Science* **300**, 108–112 (2003).
39. Knoers, N. V. Gitelman syndrome. *Adv. Chronic Kidney Dis.* **13**, 148–154 (2006).
40. Wang, L., Dong, C., Xi, Y. G. & Su, X. Thiazide-sensitive Na$^+$–Cl$^-$ cotransporter: genetic polymorphisms and human diseases. *Acta Biochim. Biophys. Sin.* **47**, 325–334 (2015).
41. Alguel, Y., Cameron, A. D., Diallinas, G. & Byrne, B. Transporter oligomerization: form and function. *Biochem. Soc. Trans.* **44**, 1737–1744 (2016).

METHODS

Data reporting. No statistical methods were used to predetermine sample size. The experiments were not randomized and the investigators were not blinded to allocation during experiments and outcome assessment.

Expression and purification. NKCC1 from *Danio rerio* was cloned into a modified pFastBac vector with an N-terminal maltose binding protein (MBP) tag and 3C protease cleavage site. This construct was expressed in Sf9 insect cells (Expression Systems, 94-001S; no further authentications were carried out and no mycoplasma contamination tests were performed for this study) using the baculovirus system. Cells were infected at a density of 3.5×10^6 to 4×10^6 cells per ml and culture flasks were shaken at 27 °C for 60 h. Cell pellets were frozen down at −80 °C until further use. All protein purification steps were carried out at 4 °C unless otherwise noted. Cells were lysed by osmotic shock by incubating them for 30 min in a buffer containing 20 mM Tris-HCl, pH 8.0 with 1.5 μg/ml leupeptin, 1.5 μg/ml pepstatin A, 1 mM benzamidine, and 1:500 dilution of aprotinin. The sample was then centrifuged at 39,000g for 20 min. The supernatant was discarded and the pellets were solubilized using a glass Dounce tissue homogenizer in buffer A (20 mM Tris-HCl, pH 8.0, 20 0mM NaCl, 200 mM KCl) supplemented with 1% lauryl maltose neopentyl glycol (LMNG, Anatrace), 0.01% cholesteryl hemisuccinate (CHS, Anatrace), 1.5 μg/ml leupeptin, 1.5 μg/ml pepstatin A, 1 mM benzamidine, and 1:500 dilution of aprotinin. The sample was stirred for 2.5 h and then centrifuged at 31,000g for 45 min. The insoluble fraction was discarded and the supernatant was incubated with prewashed amylose resin for 1 h. The resin was carefully washed to remove contaminant protein. The NKCC1 protein was cleaved from MBP by incubating with 3C protease. The sample was further purified by gel filtration (Superose 6, GE Healthcare) in buffer A with 0.06% digitonin. The peak fraction was collected and concentrated for cryo-EM.

^{86}Rb$^+$-uptake assays. Wild-type NKCC1 and mutants with an N-terminal $10\times$ His-tag were transfected into HEK 293S cells (ATCC, CRL-3022; no further authentications were carried out and no mycoplasma contamination tests were performed for this study) using a pSBbi-RP vector[42] and Lipofectamine 3000 (Invitrogen) according to the manufacturer's instructions. Stable cell lines were generated for all constructs by selecting with 2 μg/ml puromycin before carrying out further experiments. Cells were maintained in 293 Freestyle medium (LifeTechnologies) supplemented with 10% FBS.

NKCC1 function was tested by measuring ^{86}Rb$^+$ uptake in HEK 293S cells grown to confluence in 6-well plates. Ninety minutes before experiments, growth medium was replaced with a low chloride, hypotonic solution of 75 mM Na-gluconate, 0.5 mM MgCl$_2$, 0.5 mM Na$_2$SO$_4$, 0.5 mM CaCl$_2$ and 7.5 mM HEPES, pH 7.4 in order to activate NKCC1. Bumetanide (70 μM) was added to certain samples as appropriate. ^{86}Rb$^+$ uptake was allowed to proceed for 1 min in a solution of 150 mM Na-gluconate, 135 mM NaCl, 5mM RbCl (2 μCi/ml ^{86}Rb$^+$, PerkinElmer), 1 mM MgCl$_2$, 1 mM Na$_2$SO$_4$, 1 mM CaCl$_2$ and 15 mM HEPES, pH 7.4. Uptake was terminated by washing three times with an ice-cold solution of 110 mM MgCl$_2$. Cells were resuspended and lysed in 1% SDS, and subjected to scintillation quantification. The biochemical behaviour, expression level and membrane localization of each mutant and the wild type were assessed (Extended Data Fig. 6b–d).

Fluorescent size-exclusion chromatography. Wild-type NKCC1 and mutants with a C-terminal eGFP tag were grown in 6-well plates until fully confluent. Cells were collected and lysed for 2 h at 4 °C in a solution of buffer A supplemented with 1% (w/v) lauryl maltose neopentyl glycol (LMNG, Anatrace), 0.01% cholesteryl hemisuccinate (CHS, Anatrace), 1.5 μg/ml leupeptin, 1.5 μg/ml pepstatin A, 1 mM benzamidine, and 1:500 dilution of aprotinin. Equal amounts of solubilized protein (based on optical density at 280 nm (OD$_{280}$)) were analysed by gel filtration (Superdex 200 increase, GE Healthcare). Fluorescence signal was monitored using an excitation wavelength of 487 nm and emission wavelength of 507 nm.

Western blotting. Stable cell lines expressing NKCC1 were grown in 6-well plates until fully confluent, and then washed with PBS and collected. Cells were then lysed for 2 h at 4 °C in a solution of buffer A supplemented with 1% (w/v) lauryl maltose neopentyl glycol (LMNG, Anatrace), 0.01% cholesteryl hemisuccinate (CHS, Anatrace), 1.5 μg/ml leupeptin, 1.5 μg/ml pepstatin A, 1 mM benzamidine and 1:500 dilution of aprotinin. The lysates were centrifuged at 15,000g for 1 h at 4 °C and the total protein concentration in the supernatant was measured. Equal amounts of total protein were mixed with SDS loading buffer and loaded onto a Mini-PROTEAN Precast Gel (Biorad). After electrophoresis, transfer and blot, membranes were probed with a mouse anti-His primary antibody (QIAGEN), followed by a donkey anti-mouse secondary antibody (LI-COR). The membrane was then imaged using the Odyssey infrared imaging system (LI-COR).

Fluorescence imaging. Cells were seeded onto Laboratory-Tek II Chambered Coverglass (Nunc) 24 h before imaging. Three-dimensional fluorescence imaging and deconvolution was performed on a DeltaVision OMX BLAZE system (Applied Precision-GE) equipped with three emCCDs (Evolve, Photometrics) using an Olympus UPlanApo $100\times$ (NA 1.40) oil-immersion objective. Images were acquired in emCCD-mode with a gain of 200. An OMX BLAZE v.2 imaging

system (GE Healthcare) was used to image cells. A $100\times$ 1.42 numerical aperture U-PLANAPO objective was used, and emission photons captured by an Evolve 512 emCCD camera (Photometrics). Widefield epifluorescence excitation for deconvolution datasets was with InsightSSI illuminator (488nm) and standard emission filter sets (528/48). 3D images were taken with 200 nm per slice. Deconvolution was done using SoftWorx v.7.0.0. Images were background subtracted and adjusted brightness/contrast linearly using FIJI (http://fiji.sc).

Electron microscopy sample preparation and data collection. For negative-stain electron microscopy, purified NKCC1 was diluted to 0.02 mg/ml in buffer containing 0.06% digitonin, and 2.5 μl was applied to glow-discharged copper electron microscopy grids covered with a thin layer of continuous carbon film. Grids were stained with a solution of 1.5% (w/v) uranyl formate and imaged on a Tecnai T12 electron microscope (FEI) operated at 120 kV. Images were collected at a nominal magnification of 67,000×, corresponding to a calibrated pixel size of 1.68 Å on a 4k × 4k CCD camera (UltraScan 4000, Gatan). Images were binned 2 × 2 before particle selection and further processing.

For cryo-EM, 3 μl of full-length or N-terminal truncated NKCC1 purified in digitonin at a concentration of 7.6 mg/ml was applied to Quantifoil R2/1 holey carbon grids, and blotted for 2.0 s at 96% humidity on a Leica EM GP2 before being plunge frozen in liquid ethane cooled by liquid nitrogen. Grids of full-length NKCC1 were imaged on a Titan Krios operated at 300 kV. Images were collected on a K2 Summit detector in super-resolution counting mode at a magnification of 130,000×, corresponding to a physical pixel size of 1.06 Å. Data were collected using image shift to collect five images per hole. Grids of N-terminal truncated NKCC1 were imaged on a Titan Krios operated at 300 kV. Images were collected on a K2 Summit detector in super-resolution counting mode at a magnification of 130,000×, corresponding to a physical pixel size of 1.04 Å. Data was collected using image shift to collect four images per hole.

Cryo-EM data processing. Dose-fractionated super-resolution movies collected on the K2 Summit direct electron detector were binned over 2 × 2 pixels, and then subjected to motion correction using the program MotionCor2[43]. A dose-weighted sum of all frames from each movie was used for all image processing steps except for defocus determination. Defocus values were calculated using the program CTFFIND4[44] using the summed images from all movie frames without dose weighting. Semi-automated particle picking was performed using a procedure implemented in Simplified Application Managing Utilities of EM Labs (SAMUEL)[45]. Two-dimensional classification of selected particle images was performed with samclasscas.py, which uses SPIDER operations to run ten cycles of correspondence analysis, k-means classification and multi-reference alignment, or by RELION 2D classification[46]. Two-dimensional class averages were used to generate initial 3D models by SPIDER 3D projection matching refinement using samrefine.py, starting from a cylindrical density mimicking the general shape and size of NKCC1.

Three-dimensional classification and refinement were carried out in RELION 2.0 or RELION 3.0. Per-particle CTF parameter and beam-tilt refinement in RELION 3.0[47] were performed before a final run of 'auto-refine' to generate the final map of full-length NKCC1 TMD. For multibody refinement in RELION 3.0, two soft masks encompassing the TMD or soluble domain were employed. Following multibody refinement, the program relion3_flex_analyse was used to perform principal component analysis on the relative rotations and translations identified from multibody refinement[48]. All refinements followed the gold-standard procedure, in which two half datasets are refined independently. The overall resolutions were estimated based on the gold-standard Fourier shell correlation (FSC) = 0.143 criterion. Local resolution variations were estimated from the two half data maps using ResMap[49]. The amplitude information of the final maps was corrected by using relion_postprocess in RELION or bfactor.exe[50]. The number of particles in each dataset and other details related to data processing are summarized in Extended Data Table 1.

Model building and refinement. The TMD model was initially built into a 3.4 Å cryo-EM map of the N-terminal truncated NKCC1 transmembrane region using an initial template from the server RaptorX[51]. The initial template was manually rebuilt in Coot[52]. The resulting model was subsequently subject to manual adjustment in Coot against the 2.9 Å focused map of the full-length NKCC1 transmembrane region. The high quality of the maps allows unambiguous sequence register. The model of CTD was built against the 3.8 Å focused map of the full-length NKCC1 CDT region. A partial initial template was obtained from SWISS-MODEL[53] based on the MaCCC CTD structure[30], which was subject to manual rebuilding in Coot. The final CTD model contains all residues except an un-structured loop (856–925). The model for the whole molecule was generated by a rigid-body fit of the TMD and CTD models into a composite map of the TMD and CTD regions. The connection between TMD and CTD was built based on the composite map and a 4.2 Å map for the whole molecule. The models were refined using Phenix real space refine[54] and the geometry of the models was evaluated by Molprobity[55].

System setup for molecular dynamics simulations. We performed molecular dynamics simulations of single TMD protomers in a hydrated lipid bilayer, as each protomer encompasses a single ion-translocation pathway, under several different conditions. These included conditions that (1) lacked bound ions; (2) contained Na^+ and a K^+ placed in sites suggested by experimental data; (3) contained bound cations as well as two chloride ions, positioned in sites indicated by simulations of the second condition; (4) contained bound chloride ions, as in the third condition, with Na^+ also bound; (5) contained bound chloride ions, as in the third condition, with K^+ also bound; (6) contained all four ions, as in the third condition, with the Na^+ and K^+ swapped into each other's respective sites; (7) contained both cations but no bound chlorides, with Na^+ and K^+ swapped into each other's respective sites; (8) contained only bound Na^+; and (9) contained only bound K^+.

Our simulations were based on two refinements of the cryo-EM model; the two structures were remarkably similar, with very minor differences. In brief, the two refinements differed from each other in that the chloride ion within site 1 was positioned much closer to K^+ in the latter model compared to in the former model. The position of the intracellular chloride also shifted slightly. We initiated conditions 2 and 3 from models derived from both the first and second refinements and observed similar behaviour for each condition starting from either refinement. The remaining simulation conditions (1, as well as 4–9) were all initiated from the second and final refinement.

Prior to running molecular dynamics simulations of NKCC1, we performed several steps of refinement and modelling of the cryo-EM structures. Prime (Schrödinger) was used to model in missing residue side chains, and N-acetyl and N-methylamide groups were added to cap the protein termini. All titratable residues were left at their dominant protonation state at pH 7.0, except for Glu315 and Asp514, each of which had an estimated $pK_a > 7.0$, as computed by PROPKA (where pK_a is the cologarithm of the acid dissociation constant) in the second and final model. These residues are located on the extracellular face of the transporter, far from the ion-binding sites. We therefore protonated these residues in all simulations initiated from the final model. All histidine residues were represented with the hydrogen on the epsilon nitrogen. Simulations with no ions bound or with only one bound cation contained 150 mM K^+, 150 mM Na^+ and 300 mM Cl^- to increase the probability of observing spontaneous ion binding in simulation. All other simulations were prepared with 150 mM Na^+ and 150 mM Cl^-. Each of the prepared systems was inserted into a pre-equilibrated palmitoyl oleoylphosphatidylcholine (POPC) bilayer using Dabble[56]. Details on the final system sizes and corresponding simulation lengths can be found in Extended Data Table 2.

Molecular dynamics simulation force field parameters. The CHARMM36m parameters were applied to protein, the CHARMM36 parameters to lipids and ions (Na^+, K^+ and Cl^-), and the CHARMM36 TIP3P parameter set to water[57,58].

Molecular dynamics simulation protocol. Molecular dynamics simulations were performed on GPUs with the CUDA-enabled version of PMEMD in AMBER16[59,60]. Each simulation underwent a similar equilibration procedure. Following an initial minimization, each system underwent heating using the Langevin thermostat from 0 K to 100 K in the NVT ensemble over 12.5 picoseconds (ps) with 10 kcal mol^{-1} Å^{-2} harmonic restraints on all non-hydrogen atoms in the protein, ligand and lipid. Heating then continued in the NPT ensemble with semi-isotropic coupling for 125 ps and a pressure of 1 bar to a final temperature of 310 K with 5.0 kcal mol^{-1} Å^{-2} harmonic restraints. Further equilibration was then carried out at 310 K with harmonic restraints applied to the protein, as well as to ions initially present within the translocation pathway, starting at 5.0 kcal mol^{-1} Å^{-2} and reduced in a stepwise fashion every 2 ns for 10 ns, followed by a 0.1 kcal mol^{-1} Å^{-2} reduction every 2 ns for 18 additional ns for a total of 28 ns of equilibration. Production simulations were run at 310 K and 1 bar in the NPT ensemble using the Langevin thermostat and Monte Carlo barostat.

Each simulation used periodic boundaries and employed a time step of 4.0 fs using hydrogen mass repartitioning[61]. All bond lengths to hydrogens were constrained by SHAKE[62]. Short-range electrostatic and van der Waals interactions were cut off at 9.0 Å, while long-range electrostatic interactions were computed using the particle mesh Ewald method. The FFT grid size was chosen such that the width of a single grid cell was approximately 1 Å.

Snapshots from each trajectory were saved every 200 ps during the production phase of each simulation and visualized using VMD[63]. Analysis was carried out using a combination of VMD, CPPTRAJ, and locally developed analysis tools.

To quantify the occupancy of bound ions in simulation, 'grid' analysis in CPPTRAJ was used to determine the probability densities for sodium, potassium and chloride for each simulation condition[64]. A three-dimensional grid consisting of $100 \times 100 \times 100$ voxels with a spacing of 0.5 Å in each direction was constructed centred at the origin of the system (centre of the protein core). The analysis was performed on all frames, using the bincentre and normframe grid analysis options. Visualization of the resulting ion probability density was done in PyMOL, with ion densities from representative simulations in Fig. 4a (top, bottom), c displayed at contour levels of 0.0004, 0.001 and 0.001, respectively,

where a voxel with a contour level of 0.01 would contain an ion in at least 1% of all analysed simulation frames.

To quantify the distance of ions from each ion-binding site, we manually selected, for each site, a set of protein atoms whose centre represented the centre of that site, updating these coordinates for every simulation frame (K^+ site: carbonyl oxygens of Asn220 and Pro417; Na^+ site: carbonyl oxygens of Leu219 and Trp222, and side-chain oxygens of Ser538 and Ser539; extracellular chloride-binding site: amide nitrogens of Gly223 and Met225, and side-chain oxygen of Tyr454; intracellular chloride-binding site: amide nitrogens of Gly421 and Leu423, and side-chain oxygen of Tyr611; transient, intracellular chloride-binding site: C$_\gamma$ atoms of side chains at positions Asn220, Asn427 and Arg216). We then identified the ion closest to each centre of a selection of ions of a particular type. To determine ion stability within each site, we used cutoffs of 3 Å. For the swapped-cation conditions, the position of K^+ was measured with respect to the centre of the Na^+ binding site whereas the position of Na^+ was measured with respect to the centre of the K^+ binding site, as described above. Since more than one chloride could enter the translocation pore at once, we also checked whether the closest ion for one site was the same ion as for another site or for all three sites to prevent the double counting of ions. For ion-stability measurements in Extended Data Fig. 8 all comparisons were performed on simulations started from the most recent model (described above).

Reporting summary. Further information on research design is available in the Nature Research Reporting Summary linked to this paper.

Data availability

The three-dimensional cryo-EM density maps have been deposited into the Electron Microscopy Data Bank under accession numbers EMD-0470, EMD-0471, EMD-0472, EMD-0473, EMD-0474 and EMD-0475. The coordinates are deposited into the Protein Data Bank with accession numbers 6NPH, 6NPJ, 6NPK and 6NPL. All simulation starting models and trajectories are available upon request.

42. Kowarz, E., Loscher, D. & Marschalek, R. Optimized Sleeping Beauty transposons rapidly generate stable transgenic cell lines. *Biotechnol. J.* **10**, 647–653 (2015).
43. Zheng, S. Q. et al. MotionCor2: anisotropic correction of beam-induced motion for improved cryo-electron microscopy. *Nat. Methods* **14**, 331–332 (2017).
44. Rohou, A. & Grigorieff, N. CTFFIND4: fast and accurate defocus estimation from electron micrographs. *J. Struct. Biol.* **192**, 216–221 (2015).
45. Ru, H. et al. Molecular mechanism of V(D)J recombination from synaptic RAG1–RAG2 complex structures. *Cell* **163**, 1138–1152 (2015).
46. Scheres, S. H. RELION: implementation of a Bayesian approach to cryo-EM structure determination. *J. Struct. Biol.* **180**, 519–530 (2012).
47. Zivanov, J. et al. New tools for automated high-resolution cryo-EM structure determination in RELION-3. *eLife* **7**, e42166 (2018).
48. Nakane, T., Kimanius, D., Lindahl, E. & Scheres, S. H. Characterisation of molecular motions in cryo-EM single-particle data by multi-body refinement in RELION. *eLife* **7**, e36861 (2018).
49. Swint-Kruse, L. & Brown, C. S. Resmap: automated representation of macromolecular interfaces as two-dimensional networks. *Bioinformatics* **21**, 3327–3328 (2005).
50. Lyumkis, D., Brilot, A. F., Theobald, D. L. & Grigorieff, N. Likelihood-based classification of cryo-EM images using FREALIGN. *J. Struct. Biol.* **183**, 377–388 (2013).
51. Källberg, M. et al. Template-based protein structure modeling using the RaptorX web server. *Nat. Protoc.* **7**, 1511–1522 (2012).
52. Emsley, P., Lohkamp, B., Scott, W. G. & Cowtan, K. Features and development of Coot. *Acta Crystallogr. D* **66**, 486–501 (2010).
53. Waterhouse, A. et al. SWISS-MODEL: homology modelling of protein structures and complexes. *Nucleic Acids Res.* **46**, W296–W303 (2018).
54. Adams, P. D. et al. PHENIX: a comprehensive Python-based system for macromolecular structure solution. *Acta Crystallogr. D* **66**, 213–221 (2010).
55. Chen, V. B. et al. *MolProbity*: all-atom structure validation for macromolecular crystallography. *Acta Crystallogr. D* **66**, 12–21 (2010).
56. Betz, R.M. Dabble v.2.6.3. https://doi.org/10.5281/zenodo.836914 (2017).
57. Huang, J. et al. CHARMM36m: an improved force field for folded and intrinsically disordered proteins. *Nat. Methods* **14**, 71–73 (2017).
58. Klauda, J. B. et al. Update of the CHARMM all-atom additive force field for lipids: validation on six lipid types. *J. Phys. Chem. B* **114**, 7830–7843 (2010).
59. Salomon-Ferrer, R., Götz, A. W., Poole, D., Le Grand, S. & Walker, R. C. Routine microsecond molecular dynamics simulations with AMBER on GPUs. 2. Explicit solvent particle mesh Ewald. *J. Chem. Theory Comput.* **9**, 3878–3888 (2013).
60. Case, D. A. et al. AMBER (University of California, San Francisco, 2017).
61. Hopkins, C. W., Le Grand, S., Walker, R. C. & Roitberg, A. E. Long-time-step molecular dynamics through hydrogen mass repartitioning. *J. Chem. Theory Comput.* **11**, 1864–1874 (2015).
62. Ryckaert, J., Ciccotti, G. & Berendsen, H. J. Numerical integration of the Cartesian equations of motion of a system with constraints: molecular dynamics of n-alkanes. *J. Comput. Phys.* **23**, 327–341 (1977).
63. Humphrey, W., Dalke, A. & Schulten, K. VMD: visual molecular dynamics. *J. Mol. Graph.* **14**, 33–38, 27–28 (1996).

64. Roe, D. R. & Cheatham, T. E. III. PTRAJ and CPPTRAJ: software for processing and analysis of molecular dynamics trajectory data. *J. Chem. Theory Comput.* **9**, 3084–3095 (2013).

Author contributions T.A.C. performed molecular biology, biochemistry, cryo-EM sample preparation and functional studies and assisted in preparation of the figures and manuscript. B.J.O. collected and processed negative-stain and cryo-EM data, analysed the results of multi-body refinement, and assisted in preparation of the figures and manuscript. J.Z. performed biochemistry, negative-stain, cryo-EM grid preparation and optimization, cryo-EM data collection and model building and assisted in preparation of the figures and manuscript. N.R.L., A.W. and S.A.H. performed molecular dynamics simulations, analysed data and contributed to preparation of the figures and manuscript. D.-H.C. helped with the initial electron microscopy studies. R.O.D. oversaw the molecular dynamics simulations and contributed to the manuscript preparation. M.L. oversaw the cryo-EM, assisted cryo-EM data processing and contributed to the manuscript preparation. L.F. directed the project, oversaw biochemistry, functional studies, cryo-EM sample preparation and data collection and wrote the manuscript with input and support from all co-authors.

Competing interests : The authors declare no competing interests.

Additional information
**Supplementary information** is available for this paper at https://doi.org/10.1038/s41586-019-1438-2.
Correspondence and requests for materials should be addressed to M.L. or L.F.
Reprints and permissions information is available at http://www.nature.com/reprints.
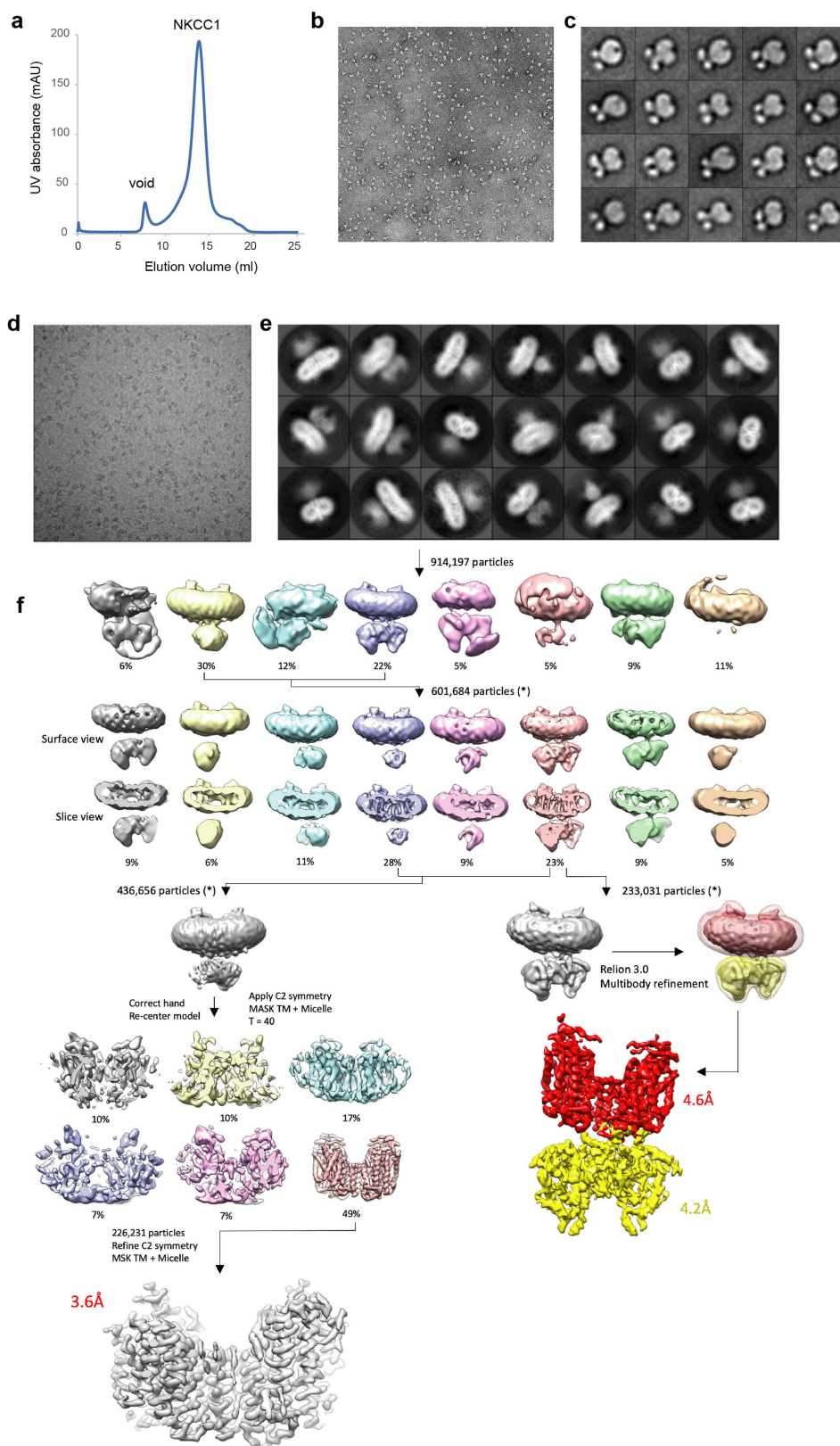
**Extended Data Fig. 1 | Biochemical characterization of NKCC1 and cryo-EM data processing workflow for N-terminal truncated NKCC1.** **a**, NKCC1 in size-exclusion chromatography. Experiments were repeated six times independently with similar results. **b**, Representative negative-stain EM micrograph of purified NKCC1 in digitonin. Experiments were repeated six times independently with similar results. **c**, Two-dimensional class averages from negative-stained particles reveal the dimeric structure of NKCC1, with two soluble domains visible beneath the TMD and detergent micelle. Experiments were repeated six times independently with similar results. **d**, Representative cryo-EM micrograph of N-terminal truncated NKCC1 particles purified in digitonin. **e**, Two-dimensional class averages of N-terminal truncated NKCC1. **f**, Classification and refinement workflow used to obtain final cryo-EM maps of N-terminal truncated NKCC1. Two processing strategies were followed to obtain a high-resolution map of the TMD (left), or a composite map of the TMD and soluble domain following Relion3 multibody refinement (right).
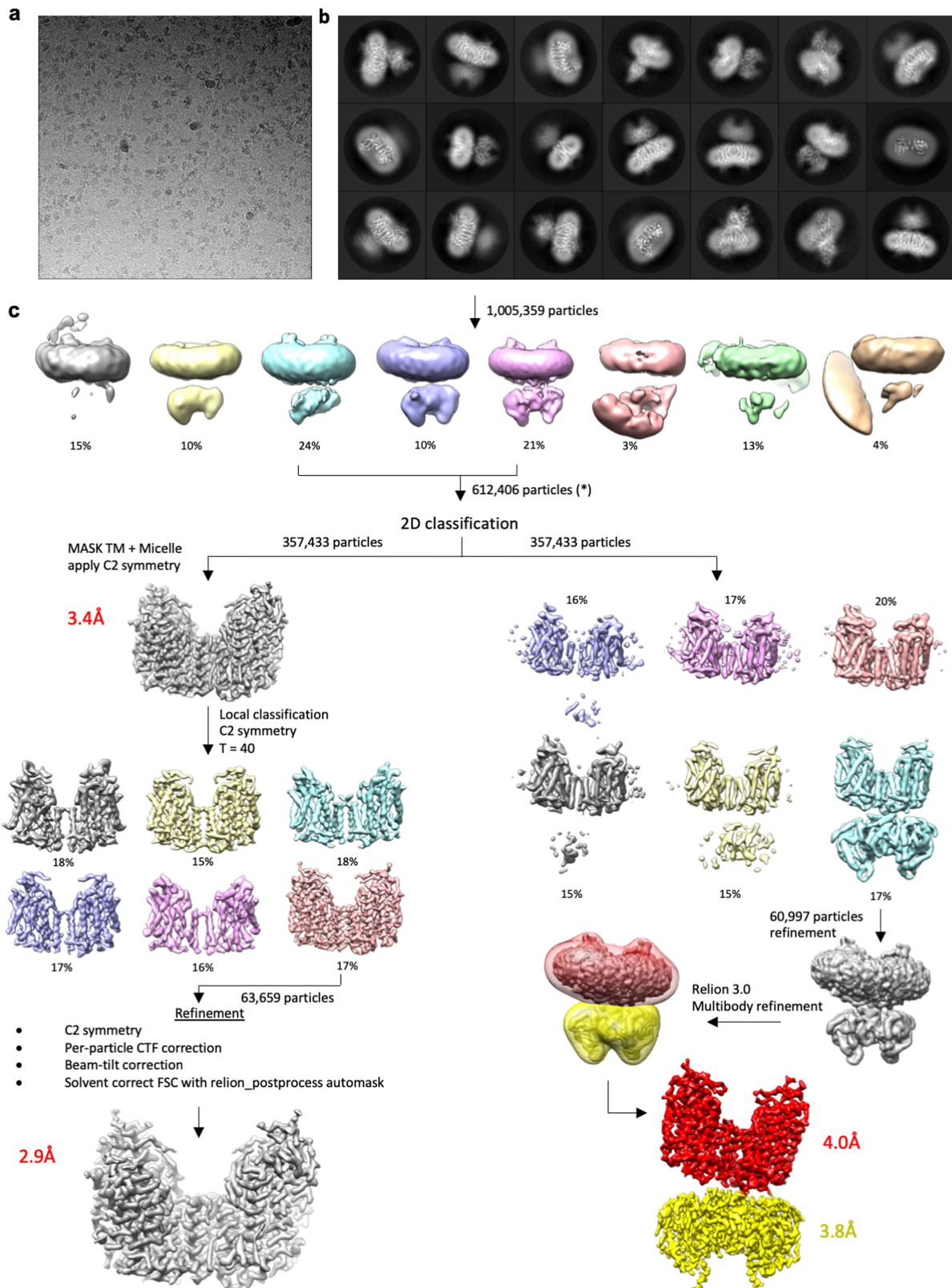
Extended Data Fig. 2 | Cryo-EM data processing workflow for full-length NKCC1. a, Representative cryo-EM micrograph of full-length NKCC1 particles purified in digitonin. **b**, Two-dimensional class averages of full-length NKCC1. Several averages show high resolution features in the TMD; however, the soluble domain is fuzzy and disordered, indicative of conformational flexibility between these two domains. **c**, Classification and refinement workflow used to obtain final cryo-EM maps of full-length NKCC1. Two processing strategies were followed to obtain a high-resolution map of the TMD (left), or a composite map of the TMD and soluble domain following Relion3 multibody refinement (right).
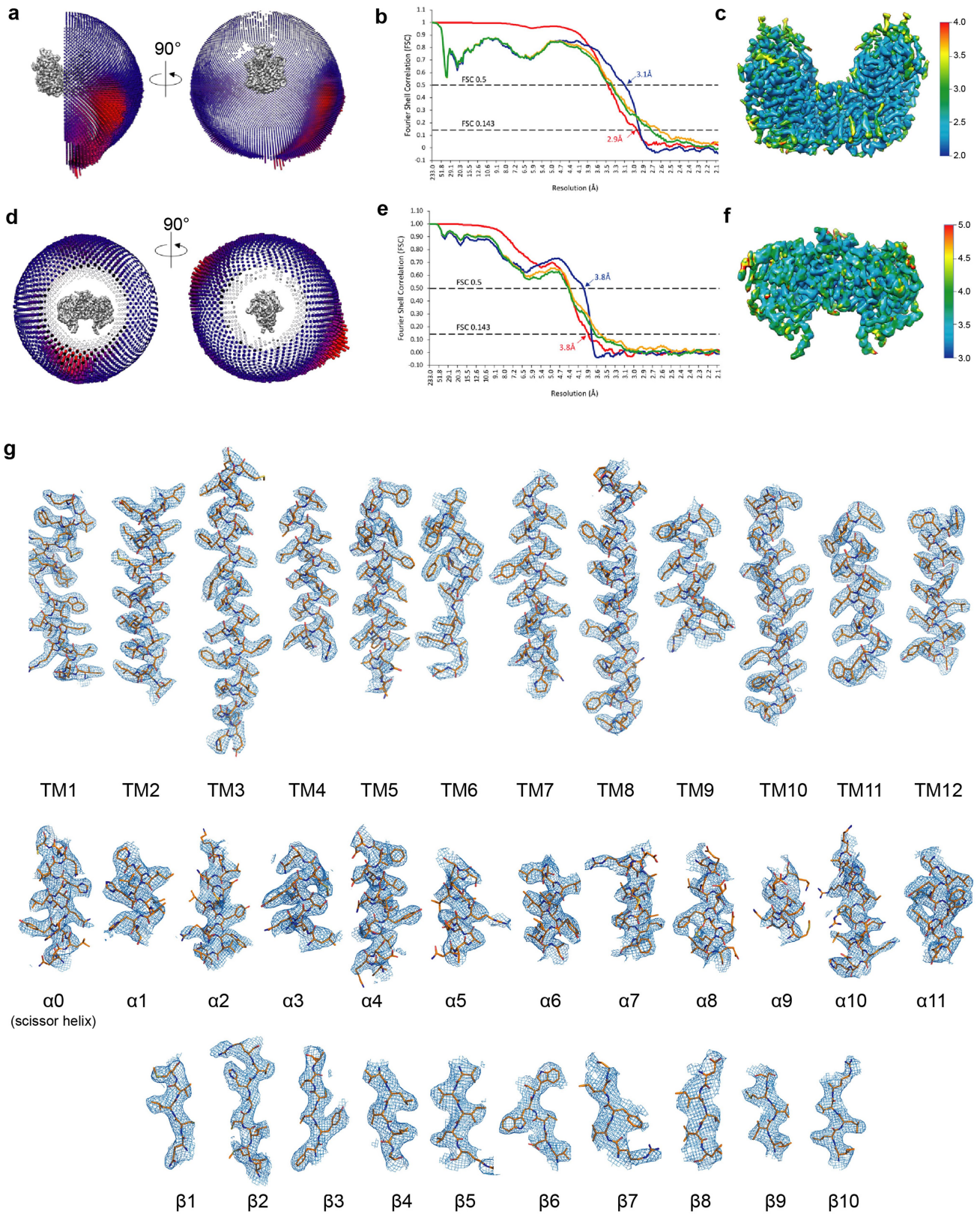
Extended Data Fig. 3 | See next page for caption.

Extended Data Fig. 3 | Cryo-EM 3D reconstruction analysis, statistics and representative density. a, Angle distributions for particles contributing to the high-resolution map of the TMD for full-length NKCC1. **b**, FSC curves: gold-standard FSC curve between the two half maps with indicated resolution at FSC = 0.143 (red); FSC curve between the atomic model of the TMD and the final map with indicated resolution at FSC = 0.5 (blue); FSC curve between half map 1 (orange) or half map 2 (green) and the atomic model refined against half map 1. **c**, Local resolution of the high-resolution TMD map as determined with ResMap. **d**, Slice view of the angle distributions for particles contributing to the map of the soluble domain for full-length NKCC1 obtained from Relion3

multibody refinement. **e**, FSC curves: gold-standard FSC curve between the two half maps with indicated resolution at FSC = 0.143 (red); FSC curve between the atomic model of the soluble domain and the final map with indicated resolution at FSC = 0.5 (blue); FSC curve between half map 1 (orange) or half map 2 (green) and the atomic model refined against half map 1. **f**, Local resolution of the soluble domain map as determined with ResMap. **g**, The cryo-EM density maps are of high quality throughout the TMD and show clear side chain features in CTD. Densities for all transmembrane helices, as well as helices and strands in the CTD are shown as wire mesh (6σ). The transporter is shown as sticks.
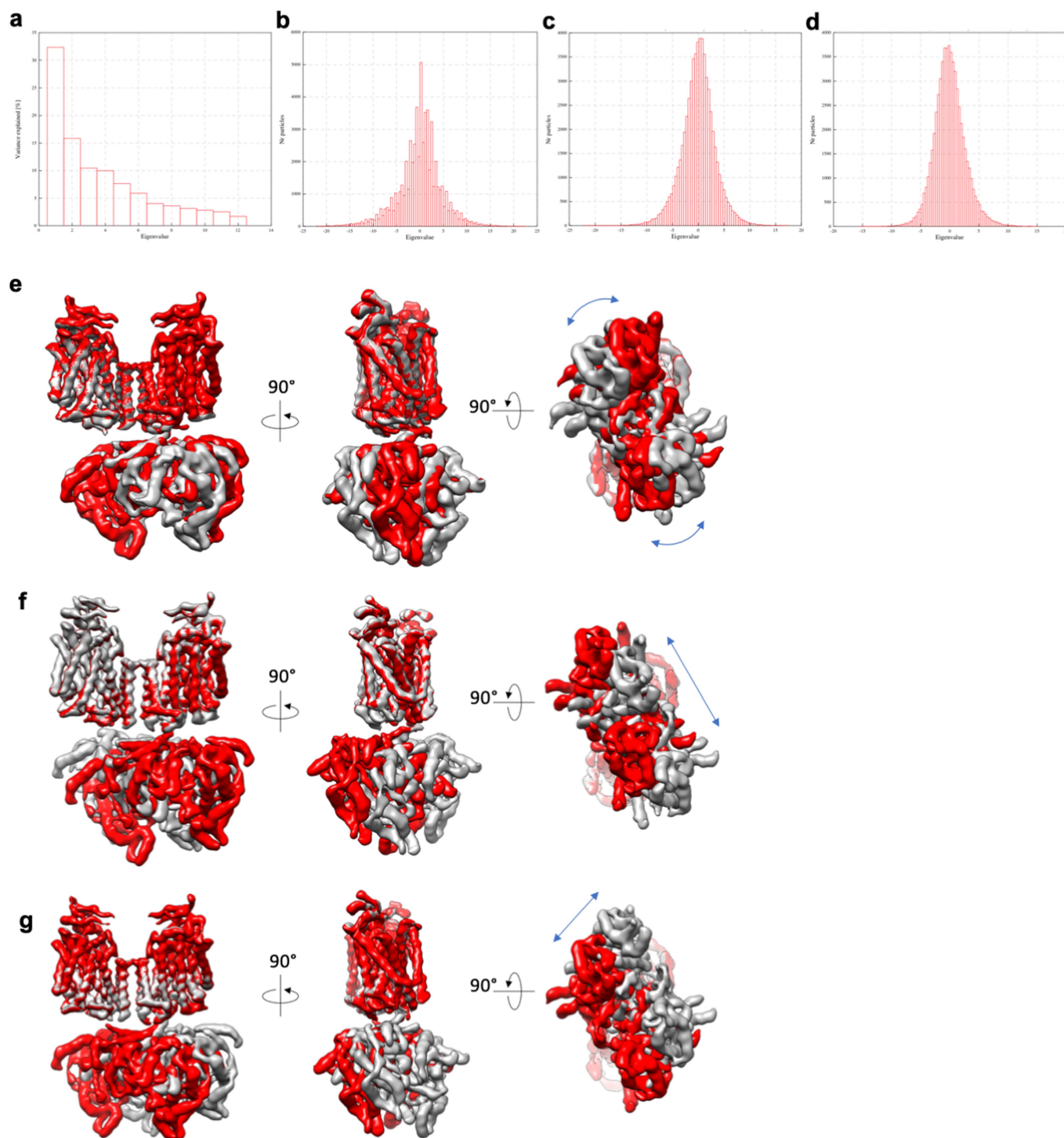
Extended Data Fig. 4 | Principal component analysis of domain movements from multibody refinement. a, Contribution of individual eigenvectors to the total variance in rotation and translation between the TMD and soluble domain. Eigenvectors 1–3 contribute more than 50% of the total variance in the rotations and translations between domains. **b–d**, Histograms of amplitude along eigenvector 1 (**b**), eigenvector 2 (**c**) and eigenvector 3 (**c**). All eigenvector amplitude histograms are monomodal, suggesting that the rotations and/or translations are continuous in nature. **e–g**, Representation of the extremes of rotation and translation between TMD and soluble domain along eigenvector 1 (**e**), eigenvector 2 (**f**) and eigenvector 3 (**g**). For simplicity of visualization, the maps at either extreme of an individual eigenvector were aligned on the TMDs. Blue arrows indicate the direction of movement of the soluble domain relative to the TMD.
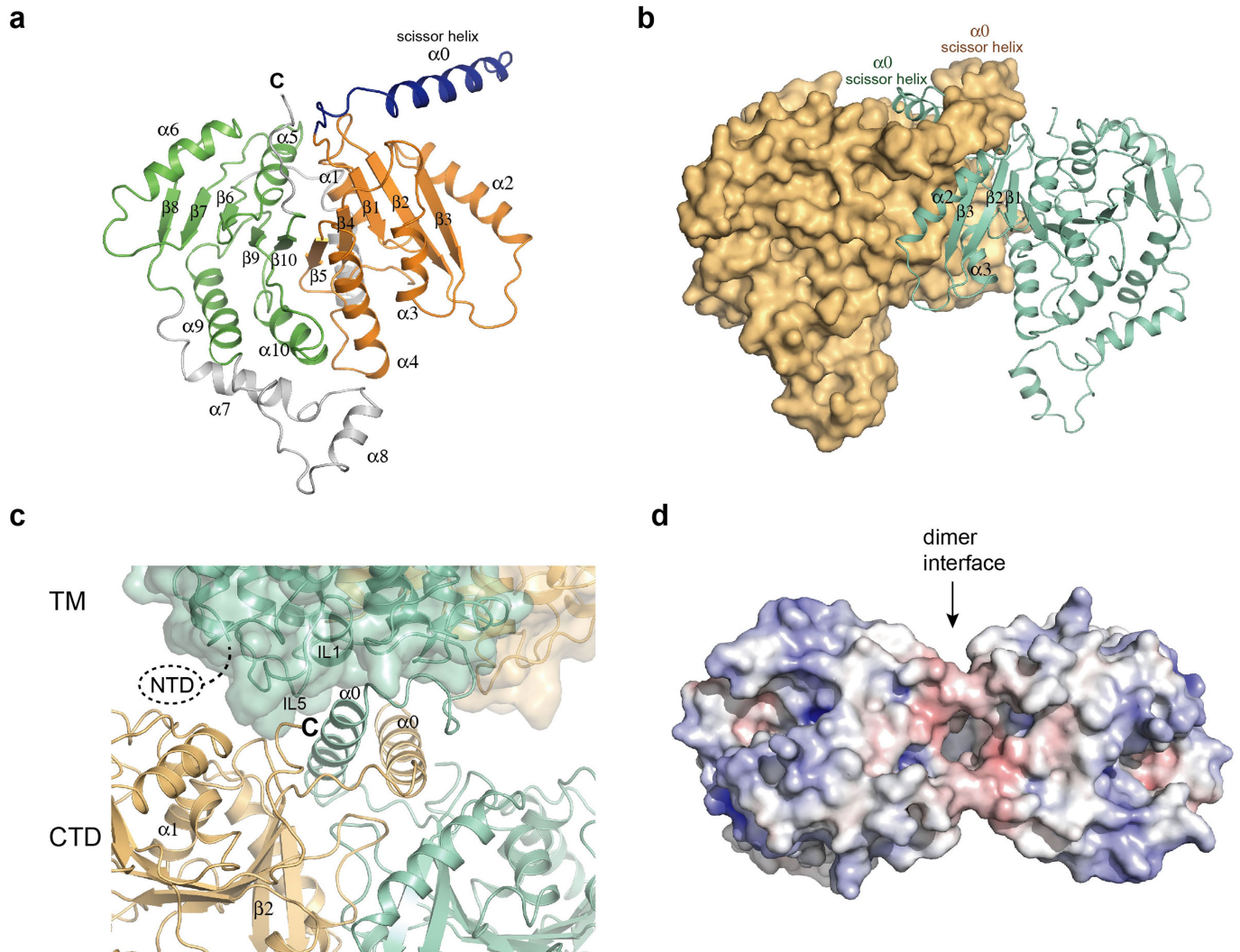
Extended Data Fig. 5 | Structure of soluble domain. a, A single subunit of the NKCC soluble domain in ribbon representation. The N- and C-terminal halves of the CTD that show a similar structure are coloured in green and orange, respectively. **b**, The dimer of the soluble domain. One subunit is shown as a surface and the other is shown as a ribbon. **c**, Close-up view of the TMD–soluble domain interface. Two subunits are coloured in dark green and gold, respectively. The TMD is shown as a surface representation and the soluble domain as a ribbon representation. The NTD and the C-terminal end of the protein are located near the interface. **d**, The intracellular surface of the TMD. The surface is coloured according to electrostatic potential (red, $-10 \, \mathrm{kT} \, e^{-1}$; blue, $+10 \, \mathrm{kT} \, e^{-1}$).
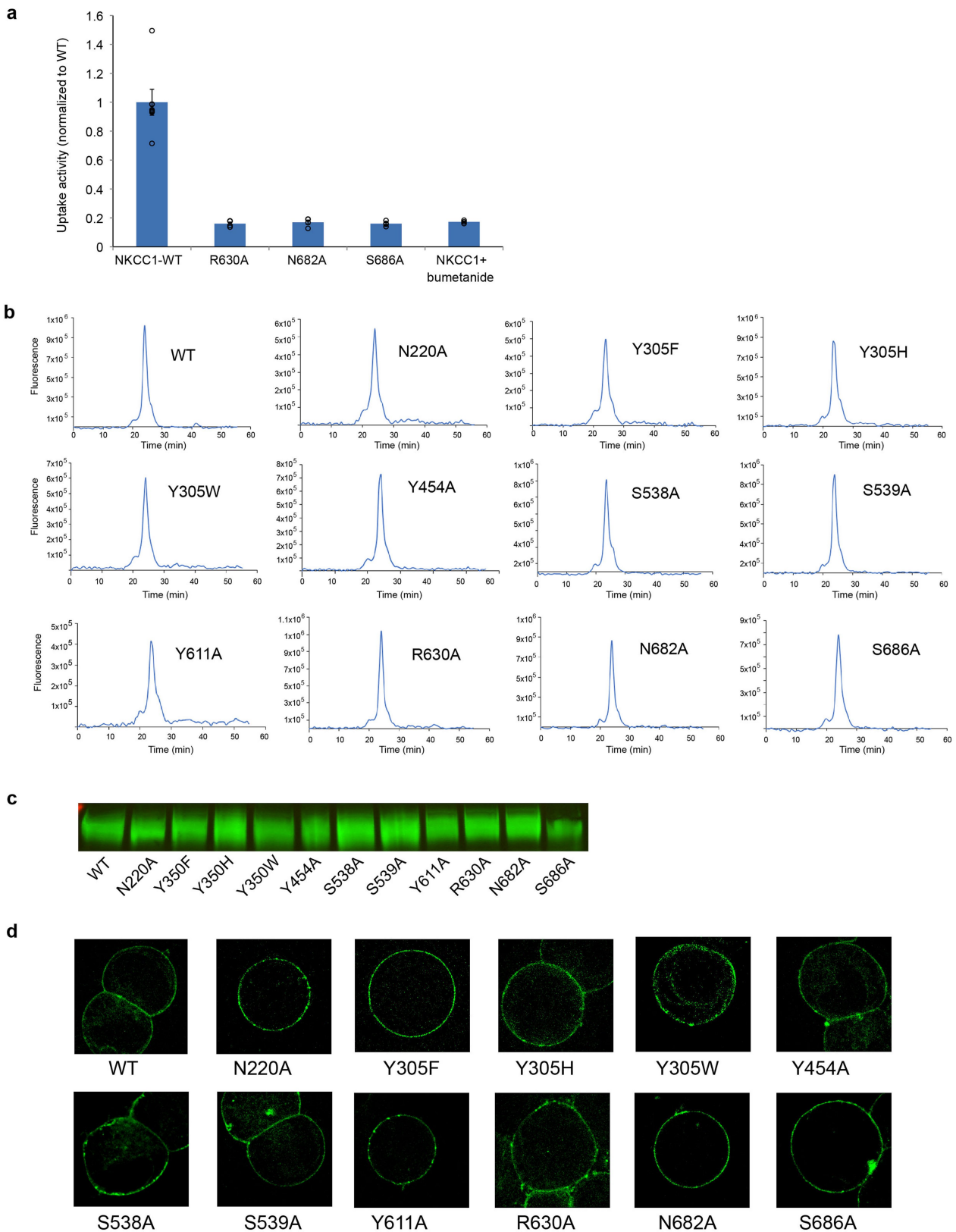
Extended Data Fig. 6 | Uptake activities of interface mutants and characterizations of all NKCC1 mutants in this study. a, Uptake activities of NKCC1 mutants at the TMD–cytosolic domain interface. $^{86}Rb^+$ uptake of NKCC1 mutants was normalized to that of the wild type (mean $\pm$ s.e.m., $n = 4$ independent experiments except for wild type, $n = 7$ independent experiments and for wild type with bumetanide, $n = 3$ independent experiments). **b**, Wild-type NKCC1 and mutants (also including those in Figs. 1e, 3e, 4f) in size-exclusion chromatography.

The GFP fusion protein is monitored by fluorescence. Experiments were repeated three times independently with similar results. **c**, The expression level of wild-type NKCC1 and mutants as shown by western blot. Experiments were repeated three times independently with similar results. For gel source data, see Supplementary Fig. 2. **d**, The membrane localization of wild-type NKCC1 and mutants. The fluorescence images are shown for HEK293 cells expressing NKCC1–GFP. Experiments were repeated three times independently with similar results.
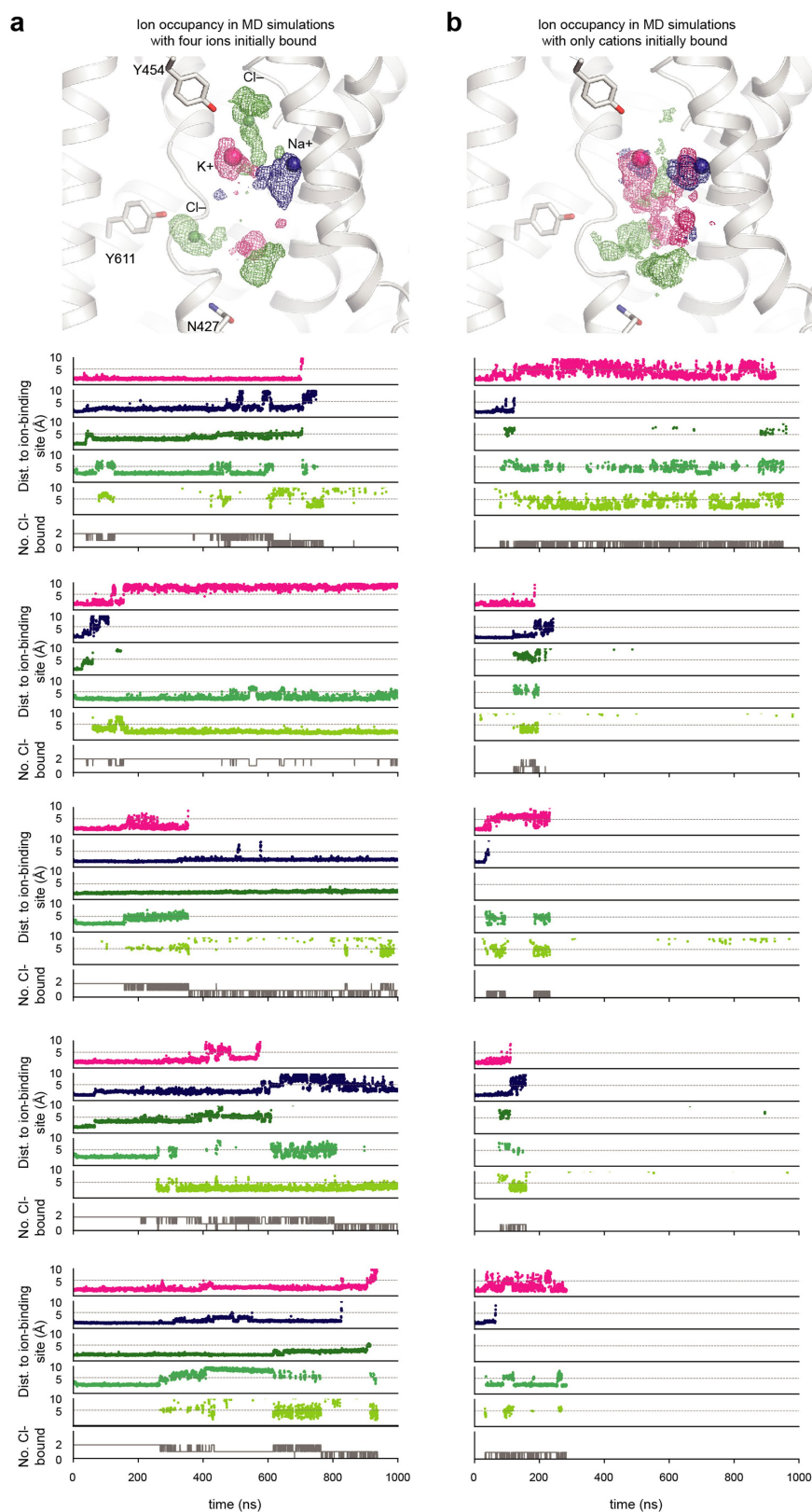
Extended Data Fig. 7 | Molecular dynamics simulations. a, Ion probability densities of ions within translocation pathway (top) and individual traces (bottom) for simulations performed with K⁺, Na⁺, and Cl⁻ initially present in the translocation pathway (model 1, see Methods). **b**, Ion probability densities of ions within translocation pathway (top) and individual traces (bottom) for simulations performed with only K⁺ and Na⁺ initially present in the translocation pathway (model 1, see

Methods). In the latter set of simulations, Cl⁻ spontaneously explores regions that form stable chloride-binding sites. Probability density maps were calculated as described in Methods. The top four simulation traces represent the minimum distance of an ion of a particular type from the pre-determined centre of each binding site (see Methods). The bottom simulation trace shows the number of Cl⁻ ions bound within any of the three chloride-binding sites at once.

Extended Data Fig. 8 | Ion stability in molecular dynamics simulations.
a–d, Comparison of relative stabilities of ions across multiple
simulation conditions. Here, stability refers to the amount of time an
ion resides within 3 Å of the pre-determined centre of each binding site
(see Methods). Each dot corresponds to a result from a single simulation.
Closed circles indicate simulations with each cation placed in its predicted
site; open circles indicate simulations with either cation swapped into
the other cation's predicted binding site. Blue circles correspond to
measurements for Na^+ and pink circles for K^+. For **a** and **b**, we examined
the relative stabilities of cations to determine whether the predicted Na^+
and K^+ binding sites exhibit a preference for their respective cations.
a, For simulations started with all ions bound, Na^+ resided longer in the
Na^+ site compared to K^+ when K^+ was initially placed within the Na^+ site
('$Na^+/K^+/2Cl^-$' vs 'Na^+/K^+ swapped, 2 Cl^-'). The same trend appeared for
simulations with just cations initially bound within the cavity ('Na^+/K^+'
vs 'Na^+/K^+ swapped'). **b**, For simulations started with all ions bound, K^+
resided for longer in the K^+ site compared to Na^+ when Na^+ was initially
placed within the K^+ site ('$Na^+/K^+/2Cl^-$' vs 'Na^+/K^+ swapped, 2 Cl^-').

For simulations with just cations initially bound, K^+ and Na^+ appeared to
leave after similar amounts of time—perhaps because, particularly in the
absence of Cl^-, the K^+ site is quite accessible to the intracellular solvent,
and ions of either type could dissociate rapidly from this area. **c**, K^+
remained within its initial position much longer compared to Na^+ in the
presence of two Cl^- ions. In simulations with Na^+ and 2 Cl^- ions bound,
Na^+ often immediately dissociated from its site, perhaps indicating that
the Na^+ site on its own has a weaker affinity for binding cations in this
state compared to the K^+ site, the increased proximity of which to Cl^- site
1 probably helps to stabilize K^+ in the site. **d**, Chloride ions spontaneously
visited and remained within 3 Å of the primary intracellular chloride
site (site 2) for longer in the presence of both cations compared to in the
presence of either cation alone. **e**, In one simulation, in which Na^+ and K^+
were initially placed in a swapped configuration with no Cl^- ions bound,
we observed escape of K^+ (pink) followed by destabilization of the Na^+ ion
(blue) within the K^+ site (123 ns) accompanied by Cl^- binding. Na^+ then
proceeded to move down towards the intracellular side (220 ns) before
rebinding for a 25-ns period within the proposed Na^+-binding site.

Extended Data Table 1 | Cryo-EM data collection, refinement and validation statistics

	Full-length NKCC1				N-terminally truncated NKCC1	
Data collection and processing						
Magnification	130,000				130,000	
Voltage (kV)	300				300	
Electron exposure (e$^-$/Å^2)	53				53	
Defocus range (μm)	1.0-3.0				1.0-2.5	
Pixel size (Å)	1.06				1.04	
Exposure time (seconds)	8				10	
Number of movies	4,586				5,845	
Initial particle images (no.)	1,005,359				914,197	

	TM domain PDB 6NPH EMDB 0470	CTD PDB 6NPJ EMDB 0471	Composite TM+CTD PDB 6NPL EMDB 0473	Full Molecule EMDB 0475	TM domain PDB 6NPK EMDB 0472	CTD EMDB 0474
Symmetry imposed	C2	C1		C1	C2	C1
Final particle images (no.)	63,659	60,997		60,997	227,231	233,031
Map resolution (Å) FSC threshold	2.9 0.143	3.8 0.143		4.2 0.143	3.6 0.143	4.2 0.143
Map resolution range (Å)	3.9-2.9	6.6-3.7		8.8-4.0	6.2-3.4	7.0-4.0
Refinement						
Initial model used (PDB code)			Individual TM domain and CTD			
Model resolution (Å) FSC threshold	3.1 0.5	3.8 0.5	3.8 0.5			
Model resolution range (Å)	233-2.9	233-3.8	233-2.9			
Map sharpening B factor (Å^2)	-107	-162		-191	-209	-250
Model composition						
Non-hydrogen atoms	7504	6186	13774		7134	
Protein residues	944	768	1722		944	
Ligands	13	--	13		--	
B factors (Å^2)						
Protein	64.27	39.82	31.72		57.11	
Ligand	65.84	--	22.94		--	
R.m.s. deviations						
Bond lengths (Å)	0.008	0.008	0.006		0.004	
Bond angles (°)	1.090	1.236	0.977		0.820	
Validation						
MolProbity score	2.26	2.47	2.62		2.21	
Clashscore	5.09	6.43	9.03		3.89	
Poor rotamers (%)	4.27	6.25	7.74		6.13	
Ramachandran plot						
Favored (%)	92.13	91.18	91.48		93.40	
Allowed (%)	7.87	8.82	8.46		6.60	
Disallowed (%)	0	0	0.06		0	

Extended Data Table 2 | Conditions and durations of molecular dynamics simulations

Simulation Condition	Initial System Dimensions (Å)	Number of Atoms	Simulation Lengths (μs)
With model 1 (see Methods)			
Na$^+$/K$^+$ bound	99 x 93 x 100	91,082	2.02, 1.52, 2.02, 2.03, 0.31
Na$^+$/K$^+$/Cl$^-$/ Cl$^-$ bound	99 x 93 x 100	91,082	2.49, 2.18, 2.07, 2.34, 2.38
With model 2 (see Methods)			
Na$^+$/K$^+$/Cl$^-$/ Cl$^-$ bound	97 x 91 x 92	81,407	2.03, 2.03, 2.04, 2.02, 2.02, 2.01, 2.01, 2.00
Na$^+$/K$^+$ bound	97 x 91 x 92	81,407	2.00, 2.03, 2.01, 2.01, 2.02, 2.03, 2.01, 2.03
Na$^+$/ Cl$^-$/ Cl$^-$ bound	98 x 92 x 92	82,679	1.43, 1.50, 1.10, 1.48, 1.39
K$^+$/ Cl$^-$/ Cl$^-$ bound	98 x 92 x 92	82,679	1.21, 1.23, 1.20 1.21, 1.01
Na$^+$/K$^+$ swapped, Cl$^-$/ Cl$^-$ bound	97 x 91 x 92	81,407	2.03, 2.01, 2.00, 2.02, 2.06
Na$^+$/K$^+$ swapped	99 x 93 x 92	84,032	2.04, 2.09, 2.00, 2.02, 2.03
K$^+$ bound	98 x 92 x 92	82,639	1.81, 1.02, 1.51, 1.40, 1.34
Na$^+$ bound	98 x 92 x 92	82,624	1.52, 1.51, 1.50, 1.01, 1.12
No ions bound	98 x 92 x 92	82,612	1.26, 1.28, 1.26, 1.47, 1.17

nature research

Corresponding author(s): Liang Feng & Maofu Liao

Last updated by author(s): Jun 14, 2019

Reporting Summary

Nature Research wishes to improve the reproducibility of the work that we publish. This form provides structure for consistency and transparency in reporting. For further information on Nature Research policies, see Authors & Referees and the Editorial Policy Checklist.

Statistics

For all statistical analyses, confirm that the following items are present in the figure legend, table legend, main text, or Methods section.

n/a	Confirmed	
☐	☒	The exact sample size (*n*) for each experimental group/condition, given as a discrete number and unit of measurement
☐	☒	A statement on whether measurements were taken from distinct samples or whether the same sample was measured repeatedly
☒	☐	The statistical test(s) used AND whether they are one- or two-sided *Only common tests should be described solely by name; describe more complex techniques in the Methods section.*
☒	☐	A description of all covariates tested
☒	☐	A description of any assumptions or corrections, such as tests of normality and adjustment for multiple comparisons
☒	☐	A full description of the statistical parameters including central tendency (e.g. means) or other basic estimates (e.g. regression coefficient) AND variation (e.g. standard deviation) or associated estimates of uncertainty (e.g. confidence intervals)
☒	☐	For null hypothesis testing, the test statistic (e.g. *F*, *t*, *r*) with confidence intervals, effect sizes, degrees of freedom and *P* value noted *Give P values as exact values whenever suitable.*
☒	☐	For Bayesian analysis, information on the choice of priors and Markov chain Monte Carlo settings
☒	☐	For hierarchical and complex designs, identification of the appropriate level for tests and full reporting of outcomes
☒	☐	Estimates of effect sizes (e.g. Cohen's *d*, Pearson's *r*), indicating how they were calculated

Our web collection on statistics for biologists contains articles on many of the points above.

Software and code

Policy information about availability of computer code

Data collection	SerialEM (v 3.7)
Data analysis	Phenix (v 1.14-3260); Coot (v 0.8.9); MolProbity (v 4.4); Pymol (v 1.5); MotionCor2 (v 1.1.0); CTFFIND4 (v 4.1.5); SAMUEL (v 17.05); SamViewer (v 16.01); SPIDER (v 17.05); RELION 3.0; ResMap (v 1.1.4); bfactor (v 1.03); Chimera (v 1.13)

For manuscripts utilizing custom algorithms or software that are central to the research but not yet described in published literature, software must be made available to editors/reviewers. We strongly encourage code deposition in a community repository (e.g. GitHub). See the Nature Research guidelines for submitting code & software for further information.

Data

Policy information about availability of data

All manuscripts must include a data availability statement. This statement should provide the following information, where applicable:

- Accession codes, unique identifiers, or web links for publicly available datasets
- A list of figures that have associated raw data
- A description of any restrictions on data availability

The three-dimensional cryo-EM density maps have been deposited into the Electron Microscopy Data Bank under accession numbers EMD-0470, EMD-0471, EMD-0472, EMD-0473, EMD-0474 and EMD-0475. The coordinates are deposited into the Protein Data Bank with accession numbers 6NPH, 6NPJ, 6NPK and 6NPL. All simulation starting models and trajectories are available upon request.

Field-specific reporting

Please select the one below that is the best fit for your research. If you are not sure, read the appropriate sections before making your selection.

☒ Life sciences   ☐ Behavioural & social sciences   ☐ Ecological, evolutionary & environmental sciences

For a reference copy of the document with all sections, see nature.com/documents/nr-reporting-summary-flat.pdf

Life sciences study design

All studies must disclose on these points even when the disclosure is negative.

Sample size	No statistical methods were used to predetermine sample size. Sufficient cryo-EM data were collected to achieve adequate map reconstructions.
Data exclusions	No data were excluded from analyses.
Replication	Each experiment was repeated at least three times in independent experiments. Experimental findings were reproduced reliably.
Randomization	This is not relevant to our study, because no grouping was needed.
Blinding	Investigators were not blinded to group allocation, because no grouping was needed for this study.

Reporting for specific materials, systems and methods

We require information from authors about some types of materials, experimental systems and methods used in many studies. Here, indicate whether each material, system or method listed is relevant to your study. If you are not sure if a list item applies to your research, read the appropriate section before selecting a response.

Materials & experimental systems

n/a	Involved in the study
☐	☒ Antibodies
☐	☒ Eukaryotic cell lines
☒	☐ Palaeontology
☒	☐ Animals and other organisms
☒	☐ Human research participants
☒	☐ Clinical data

Methods

n/a	Involved in the study
☒	☐ ChIP-seq
☒	☐ Flow cytometry
☒	☐ MRI-based neuroimaging

Antibodies

Antibodies used	Anti-mouse secondary antibody (LI-COR Biosciences, Catalog #: 926-32212, Lot #: C40910-04, 1:15,000 dilution); Anti-His mouse primary antibody (Qiagen, Catalog #: 34660, 1:2000 dilution);
Validation	Anti-His mouse primary antibody is used for western blot to detect His-tagged protein expressed in HEK293 cells. The manufacture's website states negligible cross-reactivity with crude mammalian cell lysates.

Eukaryotic cell lines

Policy information about cell lines

Cell line source(s)	sf9 (Expression Systems, #94-001S); HEK293s (ATCC, #CRL-3022).
Authentication	No further authentications were performed for this study.
Mycoplasma contamination	No mycoplasma contamination tests were performed for this study.
Commonly misidentified lines (See ICLAC register)	None of the cell lines used are listed in the ICLAC database.